Universiteit Utrecht

Photocatalytic conversion of CO₂ using perovskites stabilized with UiO-67

Daily supervisors : Christia Jabbour and Dmitrii Osadchii

First examiner : Dr. E.M. Hutter

Second examiner : Prof. dr. E.T.C. Vogt

Inorganic Chemistry and Catalysis

Debye Institute for Nanomaterials Science

Utrecht University

R.Y. van den Brink

June 1ˢᵗ, 2022

INORGANIC CHEMISTRY & CATALYSIS

Abstract

The effects of CO_2 in our air have been widely researched and the way we are generating energy and producing materials at this moment is unsustainable. A way to mitigate the CO_2 that is pumped into our atmosphere is to find a way to commercially convert it into fuels or valuable chemicals, such as CO and CH_4, that can be used in our economy. Lately solar fuels have been getting some attention.. They can be formed by using artificial photosynthesis which is based on the reaction that plants have been performing and perfecting for millennia.

Since CO_2 is a very stable molecule, catalysts are used to enhance its conversion by minimizing the energy needed in order for the reaction to take place . One of the promising catalysts that has been researched are perovskites. Due to their ionic nature and small bandgap they are ideal for photocatalytic conversion. In this research, $CsPbBr_3$ was used as a catalyst to reduce CO_2 into CO and CH_4. However because $CsPbBr_3$ contains lead which is toxic and harmful for the environment, lead free $Cs_2AgBiBr_6$ double perovskite was explored as well.

One of the serious drawbacks of perovskites is their instability in ambient atmosphere and aqueous solutions. To make them more stable the molecular organic framework UiO-67 was used to cover the perovskite crystals. UiO-67 is a very stable molecule in aqueous environments and also has good CO_2 adsorption capabilities which will help to increase the reduction activity.

The synthesis of this UiO-67 crystal was optimised by changing reaction conditions and ratios of starting products. This resulted in a repeatable synthesis to make mesoporous structures with a high BET surface area.

To test the perovskites they were spin coated on top of a borosilicate wafer and placed in a photocatalytic cell. For the combined sample the UiO-67 layer was coated over the perovskite layer forming a heterojunction. H_2 and CO_2 gas were lead over the sample and the products were analysed with a continuous GC.

To analyse the catalysts XRD, IR, Ar-physisorption, TEM and SEM were used

Pure $CsPbBr_3$ was not unambiguously proven to be photo catalytically active but when UiO-67 was added it did catalyse the reduction of CO_2 to CO. Pure $Cs_2AgBiBr_6$ was not active. However when adding H_2O to the reaction mixture $Cs_2AgBiBr_6$ did become active.

Table of Content

1- Introduction
a- Photocatalysis

Photocatalysis is an effective and sustainable way to convert solar energy to chemical energy. In nature, green plants perform a process called photosynthesis where carbon dioxide (CO_2) and water (H_2O) are converted to carbohydrates and O_2 at room temperature [1] . Photosynthesis was the inspiration for a lot of research into novel artificial catalysts that also convert CO_2 into hydrocarbons and carbon monoxide (CO). The hydrocarbons that are formed can be used as fuels or chemical building blocks for plastics and other chemicals.
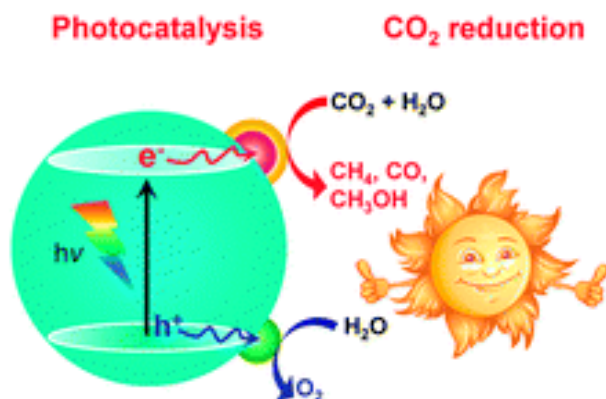

Figure 1: Main principle of photocatalytic reduction of CO_2 [2]

There are 3 main steps in semiconductor-based photosynthesis that are all shown in Figure 1. The first step is the absorption of solar photons and the conversion into electron (e⁻) and hole (h⁺) pairs. This happens when a semiconductor is illuminated by light with an energy that is higher than the bandgap. In figure x the bandgap of several semiconductors is given, an example is de bandgap of 3.2 eV for titanium dioxide (TiO_2). The second step is the charge separation and migration to reaction sites on the surface. The separation is important because otherwise the electron and hole will recombine under the emission of photons or heat. At last the chemical oxidation and reduction take place at the surface reaction sites which are induced by respectively the holes and electrons. For this step the location of the bandgap is very important because the redox potentials of the desired reactions must be located inside the bandgap.

The reduction potential of CO_2 and the oxidation potential of H_2O is shown in figure 2. These are both inside the bandgap of TiO_2 however some other semiconductors do not include both and are therefore not suitable to catalyse this specific pair of redox reactions. The reduction and oxidation reaction must both take place to prevent the accumulation of electrons or holes in the material which will destabilise and deteriorate the catalyst.
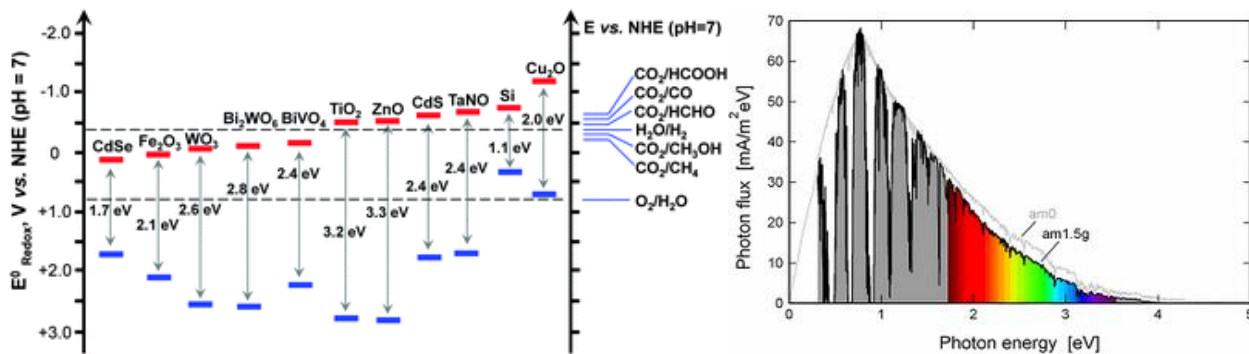
Figure 2: Band gap width and location for several semiconductors[2] and the global standard solar spectrum with the visible spectrum coloured(1.5AM).

The first photocatalyst explored in 1972 was the TiO_2 semiconductor for photolysis of water[3]. In 1979 TiO_2 was also found to be active for the reduction of CO_2 in an aqueous suspension[4]. In the following decades TiO_2 has been extensively studied in the photocatalytic field because of the low production cost and high stability. However it also has some serious drawbacks such as the wide bandgap of 3.2 eV that can only absorb photons in the UV-spectrum which means a lot of the solar energy is lost. When looking at the solar spectrum as shown in figure x most of the energy is in the visible light and infrared. So a smaller bandgap is preferred to increase the amount of energy absorbed by the catalyst. Another disadvantage of TiO_2 is the high electron-hole pair recombination rate because there is not a robust separation of charges[5].

Therefore, an efficient photocatalyst needs the following properties: good solar light absorption, efficient charge separation and good catalytic efficiency on the reaction surface. However for good solar light absorption a small bandgap is needed but a small bandgap cannot catalyse a lot of redox reactions. So it is difficult or impossible for a single semiconductor to satisfy all requirements[6].

b- CO_2 reduction

The photocatalytic conversion that will be explored in this research is the reduction of CO_2 to CO and hydrocarbons. The coupled oxidation reactions that are used are the oxidation of H_2O and H_2. The C=O bond has a high enthalpy of +805kJ/mol which requires a lot of energy to break while H-H and O-H both have a lower bond enthalpy of 436 and 497kJ/mol respectively. So the activation of the thermally stable compound CO_2 is more important to catalyse than the H_2O or H_2 activation.

For TiO_2 the reaction pathway that is shown in Figure 3 was proposed by Anpo et al[7]. Firstly the light energy is absorbed and the formed electron and hole transfer to Ti^{4+} and O^{2-} to excite the atoms to Ti^{3+} and O^-. Then CO_2 interacts with the semiconductor to first form CO and after another step form a radical C on the surface. The H_2O also interacts with the semiconductor to form H and

OH radicals on the surface. These radicals react with each other to form CH_4, CH_3OH, H_2 and O_2. However the yield found for this reaction is rather low because the chemical interaction with absorbed species has a longer time ($10^{-8}s$-$10^{-3}s$) than the recombination time of the electron-hole pairs ($10^{-9}s$) [8].
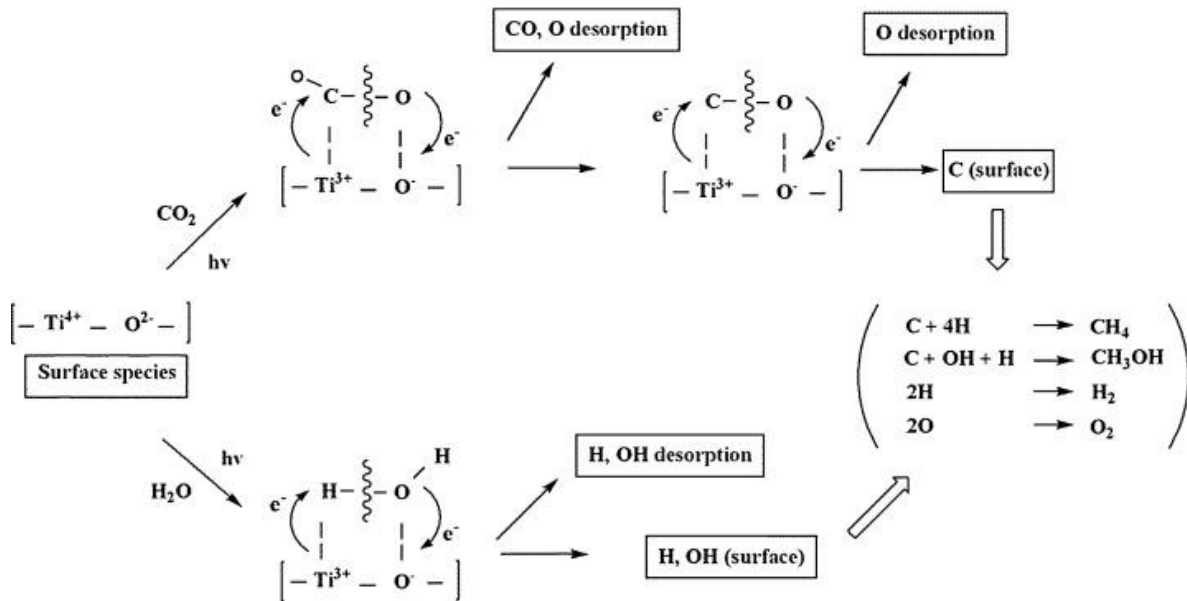

Figure 3 Reaction pathway of CO_2 and H_2O activation on TiO_2[7].

Research by Lo et al.[9] showed that H_2 can also be used as the provider of H radicals for the TiO_2 catalyst. The reduction of CO_2 with H_2 formed CH_4, CO and C_2H_6 while the photoreduction with H_2O only formed CH_4 and CO but with higher yield. When using a combination of H_2O and H_2 the product formation was almost the sum of both individual experiments. These results were obtained with a circulated solid-gas reaction.

The most promising results for CO_2 reduction have been found with a heterogenous catalyst. Two heterogenous methods are the solid-gas mode and the solid-liquid mode. Both have their strengths and weaknesses as shown in figure 4.
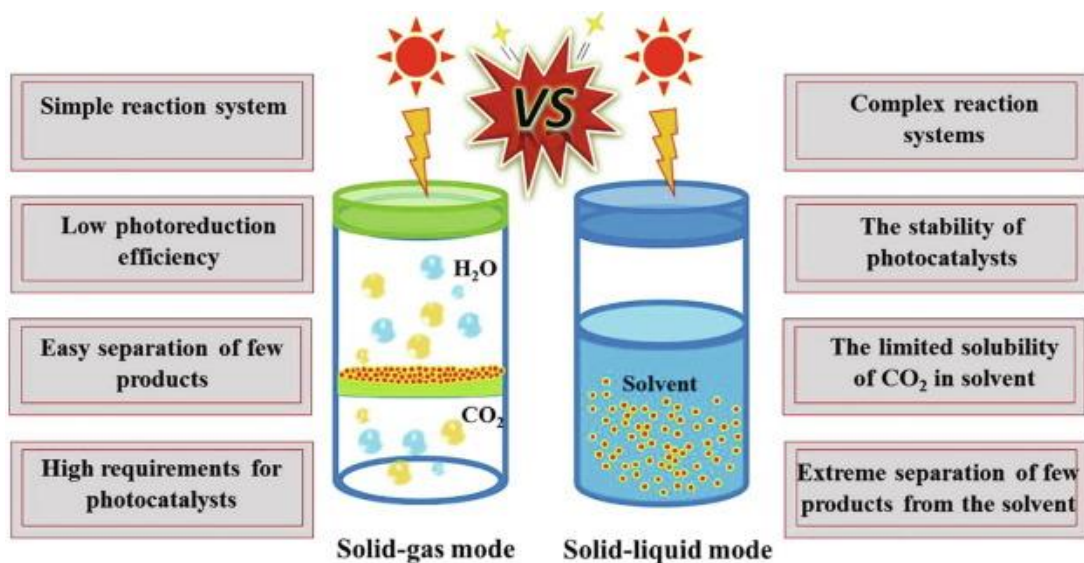
Figure 4: Comparison of heterogenous reaction conditions[10]

The solid-liquid mode has better efficiency but the separation of the products is difficult and the catalyst must be stable in the solvent. The solid-gas mode is an easier reaction system however the photocatalytic efficiency is quite low. So two of the biggest challenges in the photocatalytic field is to find stable photocatalysts in different solvents for the solid-liquid mode and to find tailored and high efficient photocatalysts for the solid-gas mode.

c- Perovskites

A very promising material for photocatalysis are metal halide perovskites (MHPs). They have an ionic structure which is ideal for charge transfer. Their general chemical formula is ABX_3 in which A and B are cations and X is a halide anion[11]. A can either be an organic or inorganic monovalent cation. The organic cations generally cause instability in the structure of the perovskite. So by replacing them with inorganic cation such as Cs^+ greatly enhances the stability [12]. Such a perovskite is also known as an all-inorganic perovskite.

An atom that is commonly found at the B site is Pb. But because of the toxic effects of Pb on the human body and the environment it would be preferred to find another suitable divalent metal element[6]. Some elements in the same group have been tested such as Sn, but this change decreases the stability of the perovskite structure [13]. So the search for lead-free halide perovskites continues.

Perovskites have been used in a number of photocatalytic reactions such as H_2 evolution [14], volatile organic compounds combustion [15], organic synthesis [16] and CO_2 conversion[17,18] [19]. The properties that explain the good photocatalytic activity are the long carrier diffusion length, strong light absorption because of the relatively small bandgap and efficient charge separation in the ionic structure. The challenges that perovskites still face before being suitable for widespread

7

industrial use is the stability in ambient and polar environments and the replacement of toxic lead without losing a lot of photocatalytic activity[20,21].

Quantum dots or nanocrystals have been found to be more active in photocatalysis than the bulk material due to their superior electron hole pair generation and transportation[22] . However the organic ligands that surround the NCs after synthesis have been identified to block carrier transportation and thus lowering photocatalytic activity [23,24]. So a washing step should be designed that removes the poisoning organic ligands but does not deteriorate the perovskite structure.

I. CsPbBr$_3$

One perovskite that has already proven its phenomenal capacity to absorb solar energy in the field of solar cells is CsPbBr$_3$ [25] which is shown in Figure 5.

CsPbBr$_3$ quantum dots have been tested successful for photocatalytic CO$_2$ reduction in the solid-liquid mode with a mixture of ethyl acetate and water used as solvent. Hou et al. [17] found that a large amount of water deteriorates the quantum dots so another solvent needed to be used. Ethyl acetate is chosen as a solvent because it has a high solubility for CO$_2$ and no obvious influence on the stability of the quantum dots. The optimal size for the quantum dots was 8.5nm and these catalysts resulted in an electron yield of 20.9 µmol g^{-1} h^{-1} towards CO$_2$ reduction. Where the equation for R$_{electron}$ = 2R$_{CO}$ + 8R$_{CH4}$ + 2R$_{H2}$ is a measure of how many electrons are used to form the products CO, CH$_4$ and H$_2$. In Table 1 a couple of examples of pure CsPbBr$_3$ NCs used as a catalyst for CO$_2$ photoreduction reaction are shown.

Table 1: Summary of reaction conditions, stability and efficiencies of pure CsPbBr$_3$, Cs$_2$AgBiBr$_6$ and combination catalysts for CO$_2$ photoreduction in different reaction modes.

Catalyst	Reaction conditions	Reaction mode	Light Source	Stability	Efficiency (R$_{electron}$ in µmol g^{-1} h^{-1})	Ref
CsPbBr$_3$ NCs 8.5nm	Ethyl acetate/water (0.3vol%)	Solid-liquid	300 W Xe lamp (AM 1.5G)	>8 h	20.9	[17]
CsPbBr$_3$ NCs/UiO-66(NH2)	Ethyl acetate	Solid liquid	300 W Xe lamp (≥420 nm)	>12 h	18.5	[26]
CsPbBr$_3$ NCs 5nm	Water vapor/ CO$_2$ gas	Solid-gas	150 mW/cm^2 (AM 1.5G)	>18 h	11.14	[27]

$CsPbBr_3$ NCs@ZIF-67	Water vapor/CO_2 gas	Solid-gas	150 mW/cm^2 (AM 1.5G)	>18 h	29.63	[27]
$CsPbBr_3$ NCs	Ethyl acetate/water (0.3vol%)	Solid-liquid	300 W Xe lamp (AM 1.5G)	>4 h	41.65	[28]
$CsPbBr_3$ NCs@Mesoporous TiO_2 beads	Ethyl acetate/water (0.3vol%)	Solid-liquid	300 W Xe lamp (AM 1.5G)	>4 h	145.28	[28]
$Cs_2AgBiBr_6$ NCs	Ethyl acetate	Solid-liquid	150 mW/cm^2 (AM 1.5G)	>6 h	17.5	[29]
$Cs_2AgBiBr_6$ NCs	Ethyl acetate/methanol (25vol%)	Solid-liquid	150 mW/cm^2 (AM 1.5G)	-	0.125	[30]
$Cs_2AgBiBr_6$ @C_3N_4-10% NCs	Ethyl acetate/methanol (25vol%)	Solid-liquid	150 mW/cm^2 (AM 1.5G)	-	2.0	[30]

II. $Cs_2AgBiBr_6$

Lately there has been some research on the idea of double perovskites. In this case the Pb^{2+} is replaced by two different monovalent and trivalent cations that alternate in the ionic structure. Thus forming an $A_2BB'X_6$ structure. This double perovskite structure has been reported to be more stable in ambient conditions than most single perovskite structure[31].
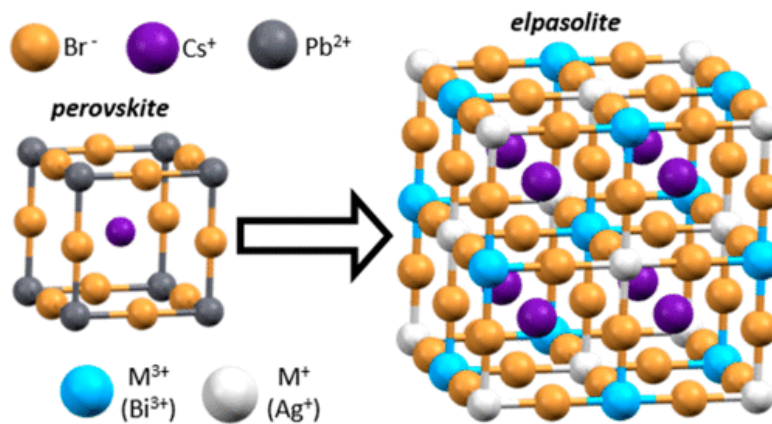

Figure 5: The CsPbBr$_3$ perovskite structure on the left and the Cs$_2$AgBiBr$_6$ double perovskite structure on the right[32].

One of the structures formed in this way was $Cs_2AgBiBr_6$ (CABB) ,shown in Figure 5, which was first reported in 2016 [33] as a replacement for the toxic lead-halide perovskites that have a high efficiency in solar cells. CABB has an indirect bandgap of 1.95 eV, a long carrier recombination lifetime and remarkable stability when exposed to moisture, heat and light. So because of this excellent photovoltaic properties it has enormous potential for photovoltaic applications such as solar cells[34,35] and photocatalysis[36].

Zhou et al. found that CABB nanocrystals have a 18.75 times higher electron yield than the bulk material. And furthermore they found that washing the nanocrystals with absolute ethanol removed most of the organic ligands on the surface that would normally block carrier transportation and reduce photocatalytic activity. This washing step resulted in a 6.5 fold increase in electron yield.

d- Combination

The photocatalytic efficiency of perovskites on their own is still too low to be used for practical applications. A way to enhance the efficiency is to combine the perovskites with another material and hereby creating a heterojunction [37]. When the perovskite is combined with a more stable material it will also ,to some degree, protect the perovskite structure to from light, heat and moisture degradation. Some materials that have been combined with perovskites for photocatalysis are: other semiconductors such as TiO_2 mesoporous beads [28] , graphene oxide [14,38,39] , Zeolitic Imidazolate Frameworks (ZIFs) [27], and metal organic frameworks (MOFs) [26]. The increase in photocatalytic efficiency is due to better charge separation and an increase in reactive sites on the surface in a heterojunction catalyst.
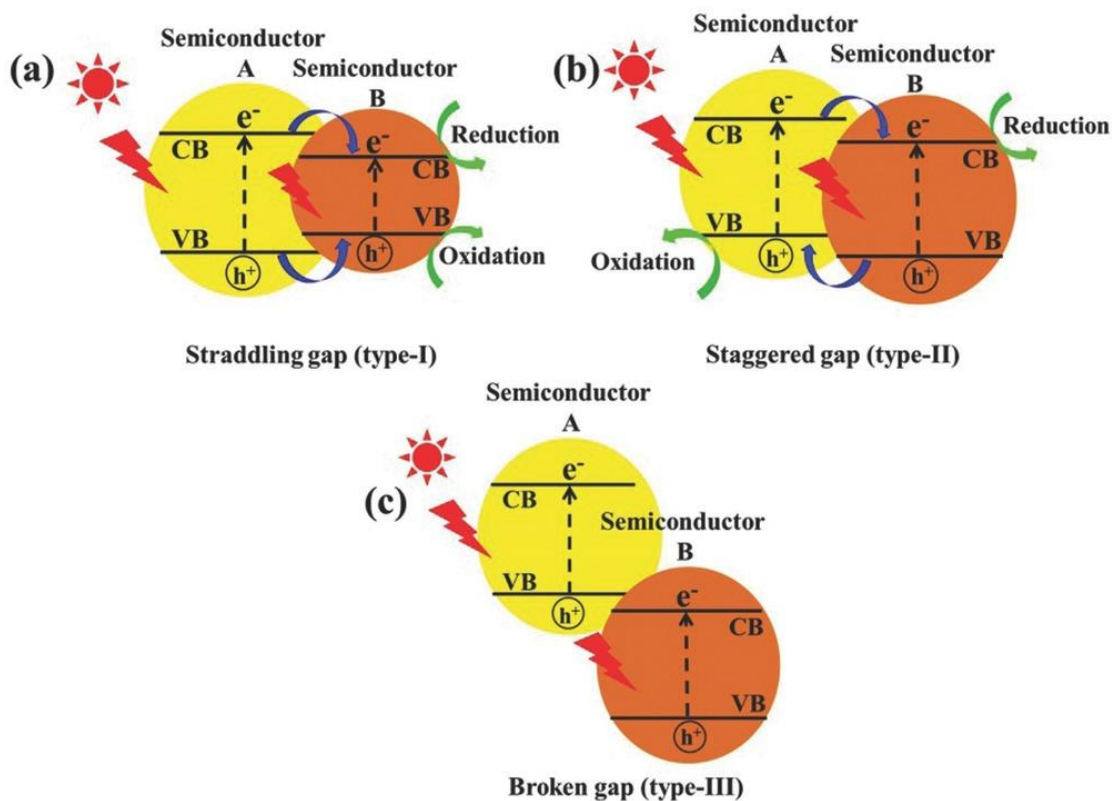
Figure 6: Different types of heterojunctions formed by combining different semiconductors [40].

There are multiple possible types of heterojunctions depending on the positions of the valence band and conduction band of both semiconductors. The first type is shown in Figure 6(a) and is called the straddling type. Here the bandgap of semiconductor B is totally inside the bandgap of semiconductor A. Both semiconductors produce carriers under illumination but after they are generated the holes and electrons will both transfer to semiconductor B where they will recombine. Type II heterojunctions are considered the best type for photocatalysis because here the electrons will transfer to semiconductor B and the holes will transfer to semiconductor A which results in good charge separation [6,41]. And finally in type III the band gaps do not overlap and there will be no significant charge transfer between the semiconductors.

However there are also some effects of the type II heterojunction that are not desired for an ideal photocatalyst. The better charge separation comes at a cost when considering thermodynamics. In the chapter on photocatalysis it was shown that the redox potential of semiconductors is very important to properly catalyse the desired reaction. In a type II heterojunction the electrons transfer to a lower conduction band and the holes transfer to a higher valence band. This reduces the redox ability of those electrons and holes[42]. When looking at a dynamic perspective the increase localisation of electron and holes will repel further transfer of electrons and holes to these sites[41]. Two adjustments of this type II have been developed to counter these drawbacks and will be discussed in next chapters.

i. Z scheme

In 1979 the Z-scheme heterojunction was proposed by Bard [43] and it was based on the principle of photosynthesis. In Figure 7 the combination of photocatalyst 1 (PS I) and photocatalyst 2 (PS II) are shown during a photocatalytic reaction. The difference with a normal type II heterojunction is that PS I and PS II are not in physical contact with each other but an acceptor/donor pair (A/D) is situated in between them that acts as a gateway for electrons from the CB of PS II to migrate to the VB of PS I to recombine with the holes there. This results in an accumulation of electron and holes on the bands with higher redox potential. However this type of Z-scheme catalyst can only result in good charge migration in solution so is unsuited for the liquid-gas mode.
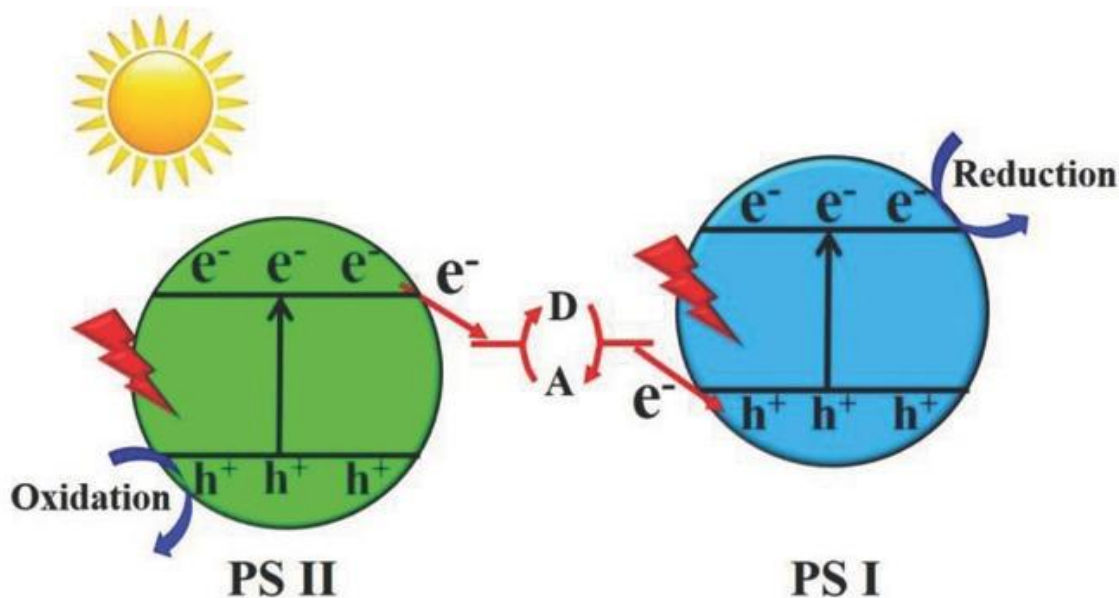

Figure 7: A schematical representation of a Z-scheme under illumination [40].

Lately a direct Z-scheme heterojunctions has been proposed by Yu et al. [44] consisting of the classical semiconductor TiO_2 and graphitic carbon nitride (g-C_3N_4). The idea of a direct Z-scheme is shown in Figure 8a. There is no need for an expensive acceptor/donor pair and the more difficult and expensive synthesis method to produce a classic Z-scheme. And a direct Z-scheme does not need to be in solution so can also be used in solid-gas mode reactions. This direct Z-scheme was achieved by loading g-C_3N_4 nanoparticles on the surface of TiO_2. However when the loading was too high the photocatalytic reaction could not take place because the TiO_2 is shielded from the sunlight so less carriers are formed, and furthermore the generated holes in the VB of TiO_2 cannot transfer to the surface and accommodate the oxidation reaction.
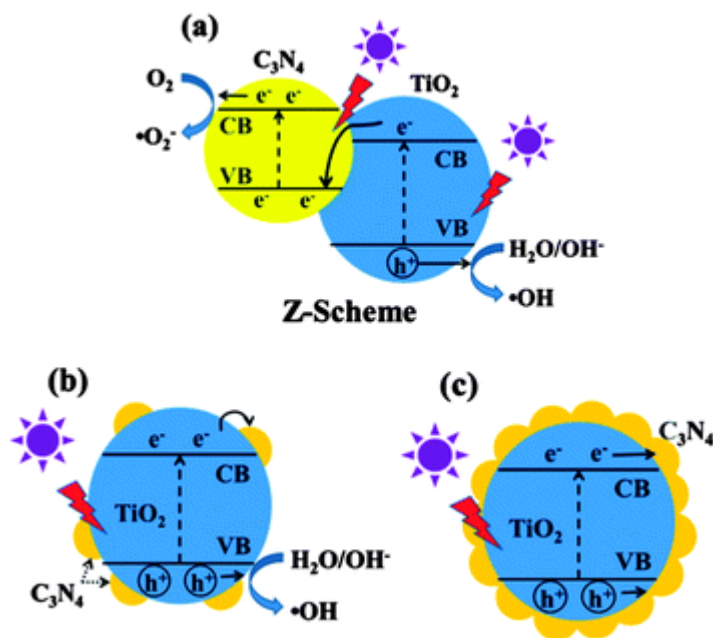
Figure 8: Schematic illustration of a direct Z-scheme (a), and a representation of the catalyst working under illumination with a low loading of C_3N_4 particles (b) and a high loading of C_3N_4 particles (c) [44].

e- Metal organic framework

Metal organic frameworks (MOFs) have great potential for stabilising perovskites and enhancing their photocatalytic activity. They are crystalline materials consisting of metal/ion clusters that are connected by organic linkers. They have been of great interest in research on H_2 [45] and CO_2 [46] gas storage, separation[47] and heterogenous catalysis[48,49]. By changing the organic linkers the pores can be finetuned for specific gasses and reactions. Furthermore the metal centres can also act as catalysts and so can the organic linkers when they are functionalised. So there is an enormous potential to finetune MOFs for a specific photocatalytic reaction[50].

Some MOFs such as UiO-66 can act as a semiconductor with transfer of carriers between the metal sites and the organic linkers[50]. Most MOFs do however have a large bandgap so they can only absorb light in the UV-spectrum. By combining them with a good absorbing perovskite this could be the perfect combination for a photocatalyst.
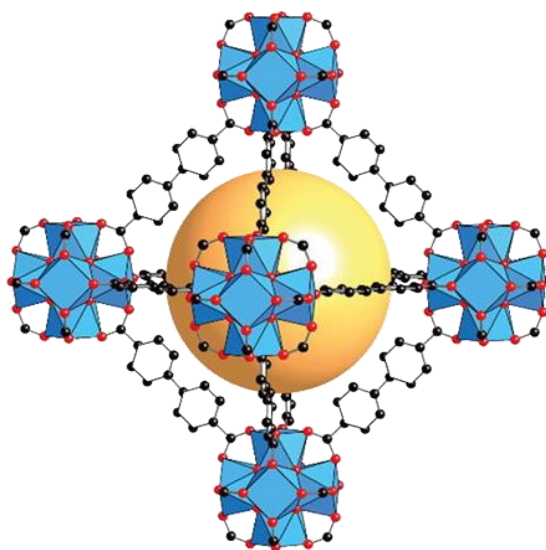
13

Figure 9: Structure of 6 Zr_6 oxo clusters linked together by 12 BPDC linkers which can be found in UiO-67 [51].
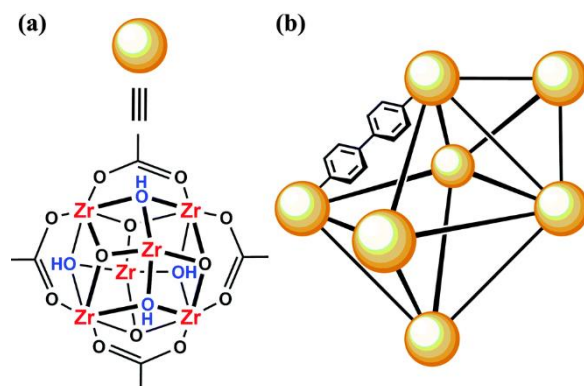

Figure 10: Structure of the $Zr_6O_4(OH)_4$ cluster with 4 of the 12 bpdc connections shown (a) and the incorporation of these structures in the MOF (b)[52].

The material that will be combined with perovskites in this study is UiO-67 which has been found in 2008 by Cavka et al. [51]. It is a porous structure with exceptional stability to temperatures up to 500°C and resistance to most chemicals. This robust framework is an ideal candidate to protect the perovskite nanocrystals from deteriorating. It consists of Zr_6 oxo clusters ($Zr_6O_4(OH)_4$) which are indicated in blue in Figure 9. These Zr_6 oxo clusters are linked together by 4,4-biphenyl-dicarboxylate (BPDC) which are shown in black. This apolar linker helps to shield the pocket that is shown in yellow where perovskite crystals could be encapsulated[53]. In Figure 10 multiple Zr_6 oxo clusters are shown as yellow spheres and how they bind together.

Zirconium based MOFs have a high absorption of high energy UV-photons (that have been cited to be harmful for perovskites) and can convert them to useful photons in the visible region by

photoluminescence[54]. Furthermore, the possibility to shift from Zr^{4+} to Zr^{3+} helps to separate the charges, hence making sure that the electrons and holes can react instead of recombining.

The synthesis of UiO-67 is possible by a solvothermal method. A modulator is added to control crystal growth, particle size, morphology and reproducibility of the synthesis [55]. A modulator is a molecule with a single acid side that competes with the linker for bonds with the Zr oxo clusters, which slows down nucleation and the crystal growth rate. Some commonly used modulators are acetic acid (AA) and benzoic acid (BA). If a modulator molecule is not removed by the linker at the end of the synthesis there will be a defect in the crystal structure. This type of defect is called a linker vacancy. This will result in more mesopores which have been shown to be beneficial for catalysis [56].

The perfect UiO-67 structure with no defects has ratio of 1:1 between Zr to linker. However when synthesising with this ratio not all the linker ends up in the structure. When using acetic acid as a modulator Gutov et al. [57] found that the ratio of Zr to linker ended up being 1 : 0.8 with a particle size of 350nm. When benzoic acid was used as a modulator the ratio was 1 : 0.35 with a particle size of 7500nm.

Another way to influence the synthesis is to add aqueous additives such as water or hydrochloric acid (HCL) to the reaction mixture. Strong acids can protonate the linker which inhibits particle formation [58]. Water and HCL have also shown to increase the rate in which MOF crystals are formed by increasing the solubility of $ZrCl_4$ in DMF [59].

Wan et al.[26] researched a $CsPbBr_3$/UiO-67(NH_2) heterojunction as a photocatalyst for CO_2 reduction. UiO-66 has t[26]he same Zr_6-oxocluster as UiO-67 but a smaller organic linker that has been functionalised with a NH_2 group (2-amino-1,4-benzene-dicarboxylate). This combined catalyst formed a heterojunction that is shown in Figure 11 which had a significant better conversion rate of CO_2 compared to both individual materials.
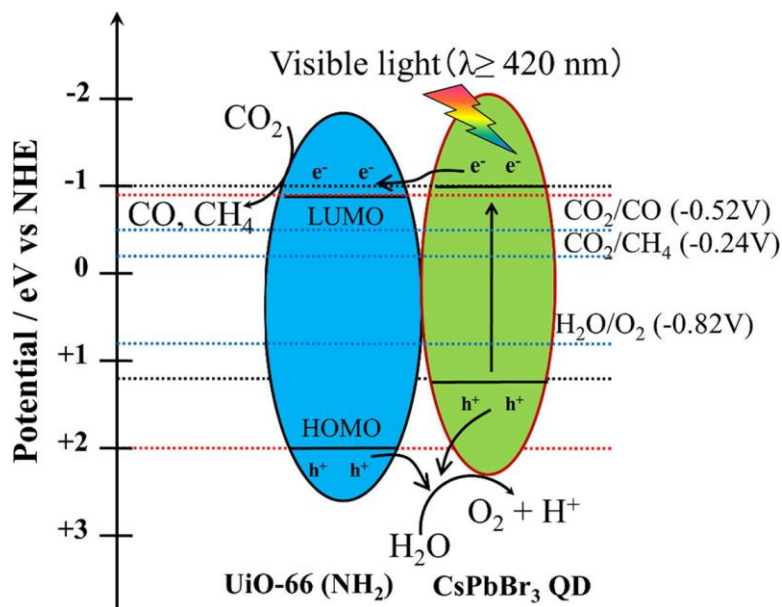
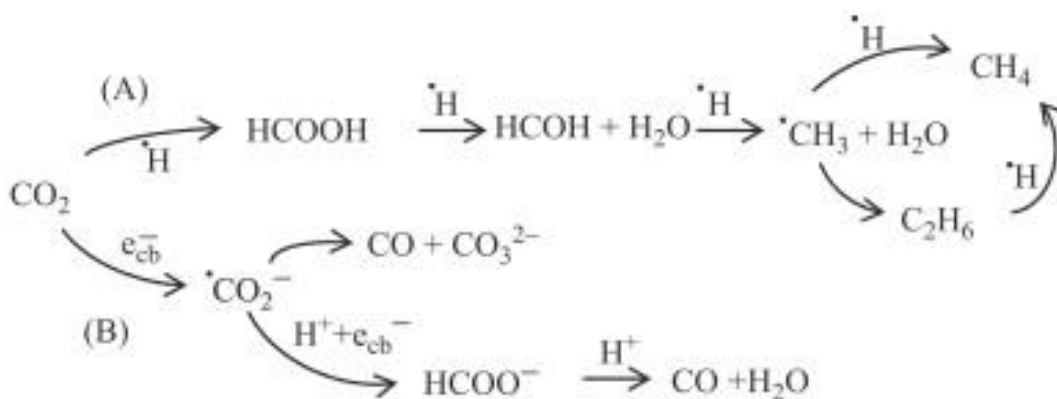*Figure 11: The CsPbBr₃/UiO-66 (NH₂) heterojunction with carrier transfer and redox reaction potentials.*

Figure 12: CO₂ reaction mechanism over TiO₂ [9]

f- Mechanisms

The exact mechanism of photocatalytic reduction of CO_2 still remains unclear however there have been multiple reports on possible mechanisms. For the CO_2 to be photo catalytically reduced it first has to be adsorbed to the surface of the catalyst. Here it can be activated by reacting with an electron to form a carbonate anion radical as is shown in route B in Figure 12. Then it can directly react to CO or further react with $2H^+$ and an electron in two steps to CO and H_2O. H_2 and H_2O have both shown to form *H radicals. These *H radicals can also react with the adsorbed CO_2 to form formic acid which can further react to a *CH_3 radical which can form hydrocarbons as is shown in route A in Figure 12. This mechanism was proposed for TiO_2 and only requires adsorption which could also happen on the surface of our UiO-67.

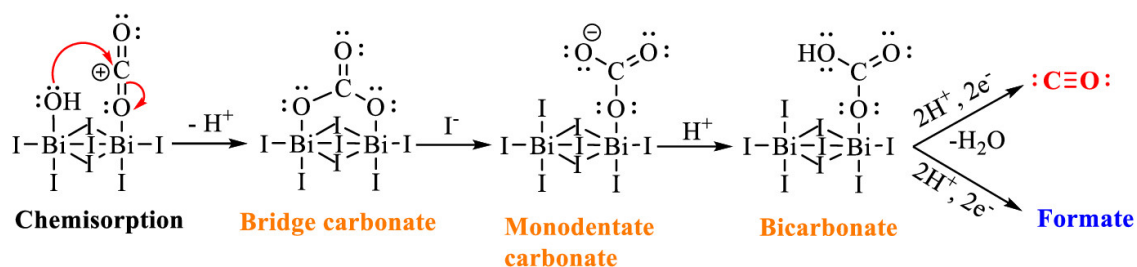The activation on perovskite catalysts is suspected to be done by chemisorption where the CO_2 molecule takes a place of one of the halogens [60]. This is shown in Figure 13 for a perovskite made up of Cesium, Bismuth and Iodide ions. The first path is the monodentate channel and can either form CO directly or via a formate intermediate. After this step there is still OH bonded to the perovskite which could react with a H^+ to form H_2O however it can also react with another chemisorbed CO_2 molecules as shown in the bidentate channel step (2). Here it can react to H_2O with either CO or formate as an additional product. The formation of methane is shown in step 3 but requires $4H^+$ and $4e^-$ to be present at the same time so this step is more difficult. Some side reactions are shown in step 4 which can form formic acid, formaldehyde and methanol.

This research aims to explore the feasibility of replacing toxic $CsPbBr_3$ with the double perovskite CABB for the application of CO_2 photoreduction. Furthermore it tests the effect of combining the perovskites with UiO-67. And it compares the solid-gas with the solid-liquid method for CO_2 photoreduction.

(1) Monodentate Channel

Chemisorption   Carbondioxy radical   Carbondioxy anion   Formate   CO formation

H^+ | e^-

Bypass channel

(2) Bidentate Channel

Chemisorption   Bridge carbonate   Monodentate carbonate   Bicarbonate   Formate
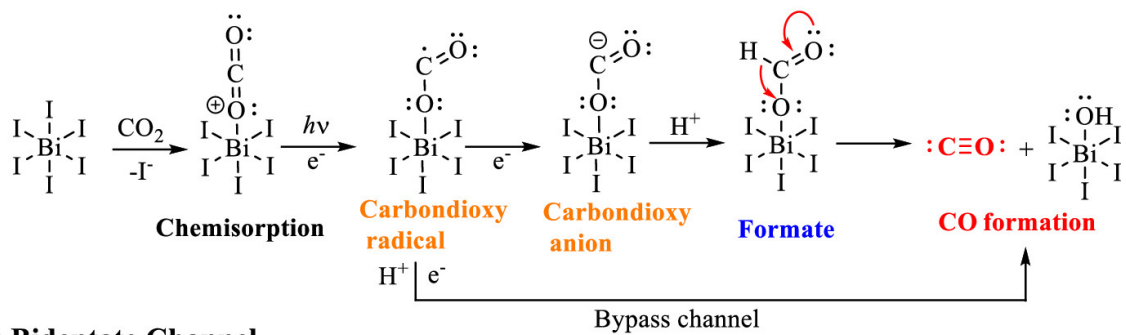
(3) Formation of methane from formate

Formate   Methoxy CH_4 formation

(4) Side reactions

(a)

Formic acid

(b)

Formaldehyde

(c)

Methanol

(d)

Water
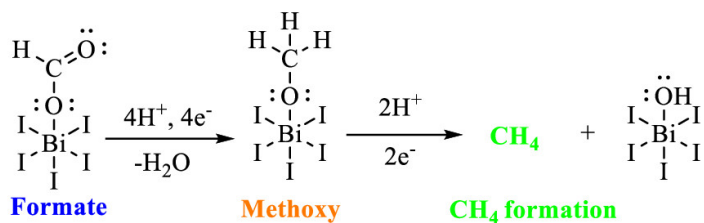
Figure 13: Reaction mechanisms over Bi based perovskite for CO_2 photoreduction [61].

2- Method

a- UiO-67 powder synthesis

Table 2: List of chemicals used for UiO-67 synthesis.

Name	Structure	Purity	Supplier
Anhydrous acetic acid (AA)	CH_3COOH	100%	Emsure
Benzoic acid (BA)	$C_7H_6O_2$	≥99.5%	Sigma Aldrich
Hydrochloric acid (HCl)	HCl	37%	Emsure
Dimethylformamide (DMF)	C_3H_7NO	≥99.8	Sigma Aldrich
Tetrahydrofuran (THF)	$(CH_2)_4\,O$	99%	Thermo Scientific
Zirconium (IV) chloride	$ZrCl_4$	≥98.0	Millipore Sigma
Biphenyl 4,4'dicarboxylic acid (BPDC)	$HO_2CC_6H_4C_6H_4CO_2H$	97%	Sigma Aldrich

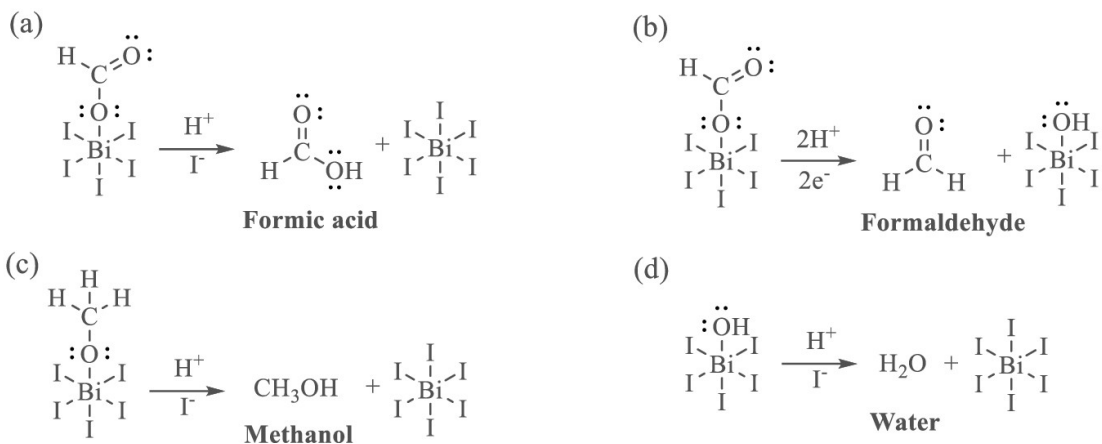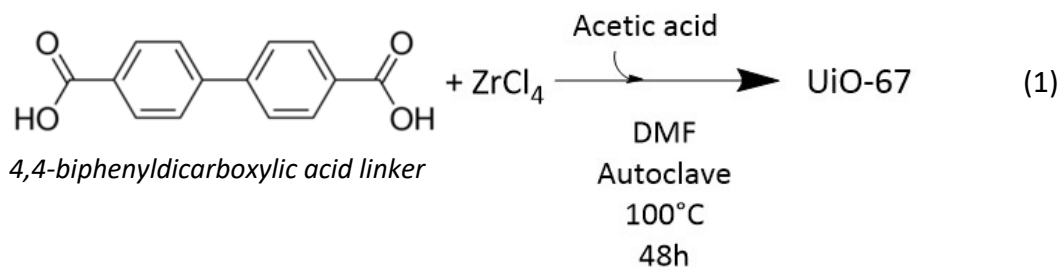A solvothermal synthesis method, that was previously reported in other methods, was used to obtain UiO-67 powder with the chemicals shown in Table 2.[53,55] $ZrCl_4$ (250mg, 1.07mmol) and different equivalent amounts of modulator (acetic or benzoic acid) were dissolved in 25ml DMF in a 100ml Erlenmeyer. The solution was heated under continuous stirring to 120°C and then an equimolar amount of the biphenyl-4,4-dicarboxylic acid (bpdc) linker (260mg, 1.07mmol) was added and heated until it dissolved. The clear solution was put in a tightly closed Teflon lined 50ml autoclave reactor and put in an oven at 100 or 120°C for 48 hours. Afterwards the reaction mixture was cooled down to room temperature and centrifuged for 5 minutes at 6000 rpm. Then the supernatant was decanted, and the powder was resuspended in 10 ml DMF by thorough shaking and centrifuged for 5minutes at 6000rpm again. This washing step was repeated 3 times with DMF and 3 times with THF before the plastic centrifugal vial is put in an

4,4-biphenyldicarboxylic acid linker

$$\text{4,4-biphenyldicarboxylic acid linker} + ZrCl_4 \xrightarrow[\substack{\text{DMF} \\ \text{Autoclave} \\ 100°C \\ 48h}]{\text{Acetic acid}} \text{UiO-67} \qquad (1)$$

oven at 80°C for an hour. Then the dried powder is taken out of the plastic vial and put in a glass vial and dried at 200°C for at least 3 hours. The washing with DMF and THF after the

solvothermal synthesis and subsequent drying steps were done to get rid of the unused linker and precursor that is left after the reaction

This conventional method has proven to be good for catalytic purposes because of a high concentration of linker vacancy defects [56]. The ideal molar ratio for a non-defect UiO-67 is 1:1 between the Zr and linker.

In the results section the effects of using a different modulator, changing the ratio of modulator to $ZrCl_4$ and using a roundbottomflask or Erlenmeyer with continuous stirring opposed to an autoclave will be discussed. The reaction conditions shown in Equation (1) are the ones that resulted in the optimal UiO-67 for the photocatalytic testing and therefore used for the synthesis of the samples that were photo catalytically tested.
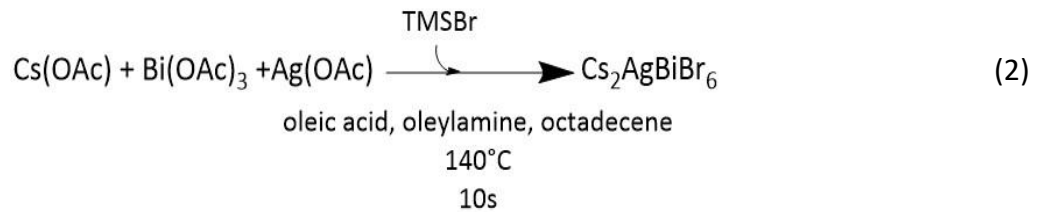
b- $Cs_2AgBiBr_6$ quantum dot synthesis

Table 3: Chemicals used for synthesis of CABB.

Name	Structure	Purity	Supplier
Cesium acetate (CsOAc)	$CsCH_3COO$	99.998%	Alfa Aesar
Silver acetate (AgOAc)	$AgCH_3COO$	99.99%	Sigma Aldrich
Bismuth acetate (Bi(OAc)$_3$)	$Bi(CH_3COO)_3$	99.999%	Alfa Aesar
Octadecene (ODE)	$C_{18}H_{36}$	90%	Acros
Oleic acid (OA)	$C_{18}H_{34}O_2$	90%	Sigma Aldrich
Oleylamine (OLA)	$C_{18}H_{37}N$	70%	Sigma Aldrich
Bromotrimethylsilane (TMSBR)	C_3H_9BrSi	≥98.0%	Merck
Toluene	C_7H_8	99.8%	Alfa Aesar
Hexane	C_6H_{14}	≥99.8%	Across

CABB quantum dot solution was synthesised by using a hot injection method as was done previously by Creutz et al.[32] Firstly CsOAc (136mg, 0.71mmol), AgOAc (83mg, 0.5mmol) and Bi(OAc)$_3$ (193mg, 0.5mmol) were dissolved in 10 ml octadecene in a 25ml roundbottomflask. 2.8ml of oleic acid was added and the reaction mixture was continuously stirred and heated to 110°C under vacuum and kept at that temperature for 45 minutes. When the reaction mixture turns from colourless to brown the atmosphere is changed to nitrogen and the mixture is heated to 140°C. 0.615ml of oleylamine is added and quickly afterwards a solution of 0.356ml TMSBR diluted in 1 ml octadecene is injected and the mixture turns yellow and turbid. After 10 seconds the reaction is cooled in an ice bath until it reaches room temperature. The reaction

mixture is centrifuged at 3700 rpm for 10 minutes. Then the supernatant is decanted, and a yellow precipitate is obtained. This precipitate is suspended in 15ml of hexane using a sonification bath and centrifuged again at 3700rpm for 10 minutes. The supernatant from this centrifugation contains a solution of CABB quantum dots.

In the results section the effect of the reaction time will be discussed however the 10s reaction was best suited for photocatalytic testing. The complete reaction that was used for the photocatalytic samples is shown in equation 2. The CABB quantum dot solution was stored in a dark box in a glovebox until further use.
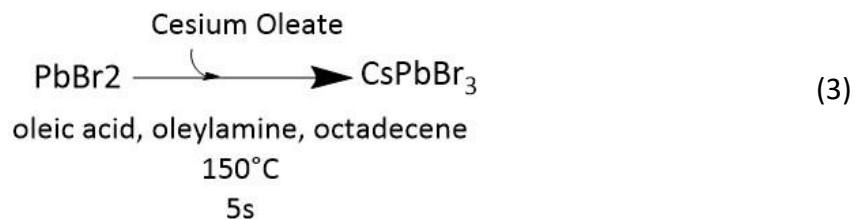
$$\text{Cs(OAc)} + \text{Bi(OAc)}_3 + \text{Ag(OAc)} \xrightarrow[\substack{\text{oleic acid, oleylamine, octadecene} \\ 140°C \\ 10s}]{\text{TMSBr}} \text{Cs}_2\text{AgBiBr}_6 \tag{2}$$

c- CsPbBr$_3$ quantum dot synthesis

Table 4: Additional chemicals used for CsPbBr3 synthesis.

Name	Structure	Purity	Supplier
Cesium carbonate	CsCO$_3$	99.9%	Sigma Aldrich
Lead(II) bromide	PbBr$_2$	99.999%	Sigma Aldrich

The CsPbBr$_3$ quantum dot solution was also synthesised by using a hot injection method that was done before in previous methods.[17,62] Firstly a 0.4M CsOL solution was prepared by mixing Cs$_2$CO$_3$ (326mg) with 3.16ml OA and 1.84ml ODE in a roundbottomflask. Then it was heated to 110°C under nitrogen atmosphere and kept at that temperature for half an hour. Then the reaction mixture was slowly put under vacuum to prevent rigorous bubbling. The mixture was kept under vacuum at 110°C for 4 hours until no more visible bubbles appeared. After backfilling with N$_2$ this CsOl solution can be stored and used in the hot injection method.

$$\text{PbBr2} \xrightarrow[\substack{\text{oleic acid, oleylamine, octadecene} \\ 150°C \\ 5s}]{\text{Cesium Oleate}} \text{CsPbBr}_3 \tag{3}$$

This ratio of 1:5 Cs:OA for the solution was found to be soluble at room temperature , and optimal for the synthesis of lead halide perovskites, by Lu et al.[63] The ratio that is mostly used in

literature leads to a insoluble mixture at room temperature and this results in inconsistent synthesis results for $CsPbBr_3$.

$PbBr_2$ (138mg, 0.376mmol) was mixed with 5ml ODE in a 25ml roundbottomflask and heated to 120°C under vacuum and continuous stirring for 1 hour. After total solubilization of the $PbBr_2$ the temperature was raised to 130°C or 150°C and 1ml of OA and 1 ml of OLA were added. 0.25ml of the 0.4 CsOl was injected and after 5 seconds the reaction mixture was cooled in an ice bath. Afterwards the sample is centrifuged at 3750rpm for 15 minutes and the precipitate was suspended in 10ml toluene by putting it in a sonification bath for 15 minutes.

In the results section the difference between 130C and 150C is shown but the reaction conditions in equation 3 were the most optimal and therefore used for the synthesis of the photocatalytic sample. The $CsPbBr_3$ quantum dot solution was also stored in a dark box in a glovebox.

d- Sample preparation

The samples were spin coated on a 2 by 2 cm borosilicate glass wafer. This method has proven to be effective for a flat microstructure with minimal roughness when using UiO-66.[64] First the wafers were pre-treated to ensure a uniform and stable layer. The wafers were first washed with water and soap, then with acetone and put in an ultrasonic bath for 15 minutes. Finally, the wafers were washed again with isopropanol and put in an ozone cleaner for 30 minutes. The cleaned wafers were immediately used for spin coating or stored in isopropanol.

The UiO-67 MOF was first suspended in toluene to get a 4.3wt% solution. The perovskite quantum dot solution was used as synthesised. In Figure 14 the process of spin coating is shown which was done in an inert glovebox.
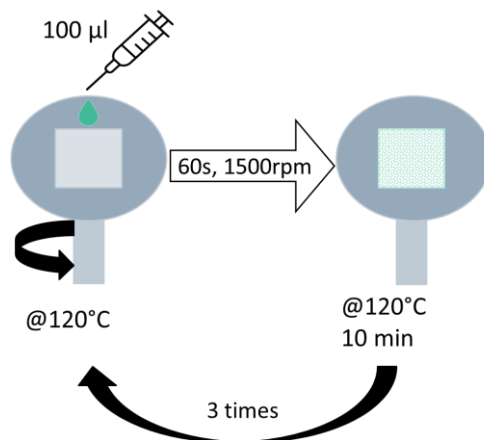

Figure 14: Spin coating method

Firs the wafer was preheated to 120°C and then 100 µl of solution was slowly dropped on the wafer while it spined around at 1500rpm for 60 seconds. Then the wafer was dried for 10 minutes at 120°C. This was repeated 3 times for every layer to get a loading of approximately

5mg. When combining the perovskite was first spin coated 3 times and afterwards the UiO-67 layer 3 times as well.

e- Characterisation of materials

X-ray diffraction (XRD)of UiO-67 were measured on a Bruker D2 phaser X-ray diffractometer using Co $K_{\alpha 12}$ radiation ((λ = 1.790 Å) in the range of 2Θ = 5 to 35°with a step size of 0.02° and a scan time of 0.5s.step. The patterns of the spin coated samples were measured on a Bruker D8 phaser X-ray diffractometer using Cu $K_{\alpha 12}$ radiation ((λ = 1.542 Å) in the range of 2Θ = 10 to 40°with a step size of 0.02° and a scan time of 0.5s/step. The results were used to see how crystalline the samples were and what phase they are in.

Infrared spectroscopy (IR) spectroscopy of the spin coated samples were recorded on a Fourier-transform infrared spectroscopy (FTIR) Perkin Elmer spectrum on with a MIR-TGS source. The results were used to identify any characteristic groups and to check what residues were left in the structure of the MOF after synthesis.

Argon Physisorption measurements were performed at -196°C using a Micromeritics Tristar 3000 instrument. From the results the BET surface area and the microporosity was calculated.

Transmission electron microscopy (TEM) images of the perovskites were taken on a TFS Talos F200X 200kv to check the particle size and form.

Scanning electron microscope (SEM) images were taken on a Phenom Pro to check if the UiO-67 crystals were

UV-VIS measurements were taken on a Cary 60 to check the light absorption properties of the quantum dot solutions.

f- Catalytic testing

An in house build continuous gas flow setup in a black box was used for the photocatalytic testing. A solar simulator lamp (Figure 15a) was used to illuminate the sample. The photocatalytic cell is shown in Figure 15b and c and has an inlet and outlet for gas on the sides and a thermocouple inlet on the top.
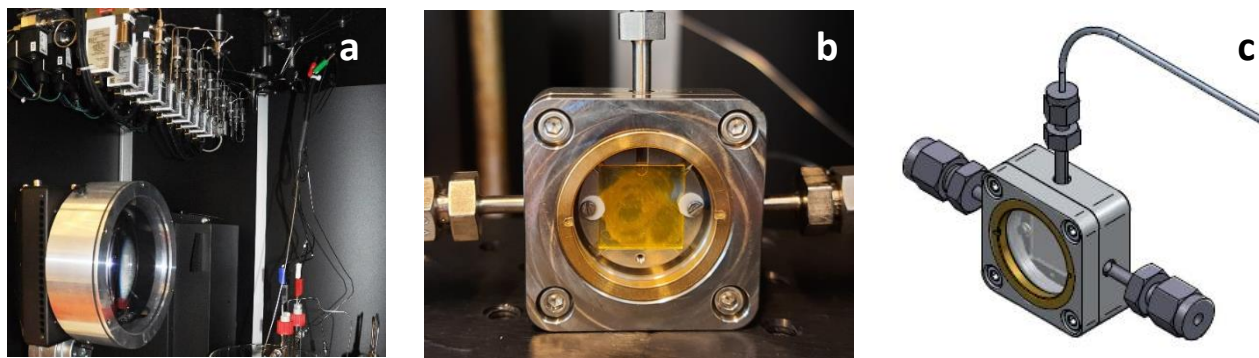
Figure 15: The solar simulator lamp (1.5AM) and the mass flow controllers(a). A sample inside the photocatalytic cell(b). A schematic drawing of the photocatalytic cell(c).

First the lines were flushed using N2 with an empty cell. Then a sample was loaded in the cell in a glovebox and the cell was connected to the lines again. Before testing the sample was flushed with 2ml/min N2 for 15 minutes. During testing a flow of CO2:H2:Kr of 1:2:0.2 ml/min was used and after a while the solar simulator lamp was turned on. All the products were analysed by a Thermo Fischer trace 1300 gas chromatograph. All the samples tested are shown in Table 5

For the CABB and TiO_2 samples an additional test was performed with a bubbler installed before the cell to introduce some H_2O in the system.

Table 5: Samples for photocatalytic testing.

Sample	Light on
$CsPbBr_3$	After 30 minutes
$Cs_2AgBiBr_6$	After 90 minutes
UiO-67#7	After 30 minutes
$CsPbBr_3$	Immediately
$CsPbBr_3$ + UiO-67	Immediately
$Cs_2AgBiBr_6$ +H_2O	Immediately
TiO2	After 30 minutes
TiO2 + H2O	Immediately

3- Results and discussion

a- Synthesis and preparation

i.   UiO-67

In Figure A1 the IR spectra of all UiO-67 samples and the pure linker is shown. The IR peaks at 2500-3000 cm^{-1} for the carboxylic acid group that are visible in the pure bpdc spectra are not visible in any of the UiO-67 IR spectra. So the washing and drying steps were sufficient to get rid of all unreacted linker.

1.   Effect of modulator

In Table 6 all the prepared UiO-67 samples are shown with the BET surface area and mesopore percentage as calculated by using the Ar-physisorption results. The combination of BA and HCL forms porous structures that can be analysed with Ar-physisorption and so does AA on its own. However the combination of AA and HCL resulted in an amorph structure without pores as is seen by the negative slope result of UiO-67#3 and #4. The combination of BA and HCL did result in porous structures just as the individual use of AA. Literature has shown that solely using BA resulted in big crystals of 7500nm [57] so the HCL was added to protonate the linker to inhibit particle formation to a certain extent. However when using AA the particles were already as small as 350nm so adding the HCL most inhibited the formation of UiO-67 crystal too much. As is confirmed by the amorph structures formed when using both AA and HCL.

Table 6: Sample list of UiO-67 synthesised with a 1:1 ratio of ZrCl$_4$ to bpdc linker in an autoclave at 120°C for 48 hours unless stated otherwise in the comments column. The BET surface area and percentage of mesopores that were calculated using the Ar-physisorption results are also shown.

Name	Modulator	Comments	BET surface area (m²/g)	Mesopore (%)
UiO-67#1	10 eq BA + HCL		1370	3.07
UiO-67#2	10 eq BA + HCL	Erlenmeyer	1596	4.89
UiO-67#3	10 eq AA + HCL	Amorph	-	-
UiO-67#4	10 eq AA + HCL	Amorph	-	-
UiO-67#5	1 eq AA	Amorph	-	-
UiO-67#6	10 eq AA		193	13.47
UiO-67#7	30 eq AA		2374	9.01

UiO-67#8	30 eq BA + HCL	Not soluble	-	-
UiO-67#9	30 eq AA	24 hours in rbf	1937	0.93
UiO-67#10	30 eq AA	48 hours in rbf	1367	2.34
UiO-67#11	30 eq BA + HCL		2434	3.53
UiO-67#12	30 eq AA		1458	36.15
UiO-67#13	30 eq AA	100°C	3162	9.96
UiO-67#14	30 eq AA	100°C	3243	25.32

To compare the synthesis of UiO-67 with AA and BA modulator we have plotted the XRD results of UiO-67#7 and UiO-67#11 in Figure 16. It can be seen that they both have very sharp peaks indicating a good crystalline structure. The peak positions are very similar only the peak intensities differ a bit. So when looking at the XRD data the crystal structures are very similar. The peak positions labelled with a + are the ones that correspond to the typical peaks observed for UiO-67 [65,55,51].
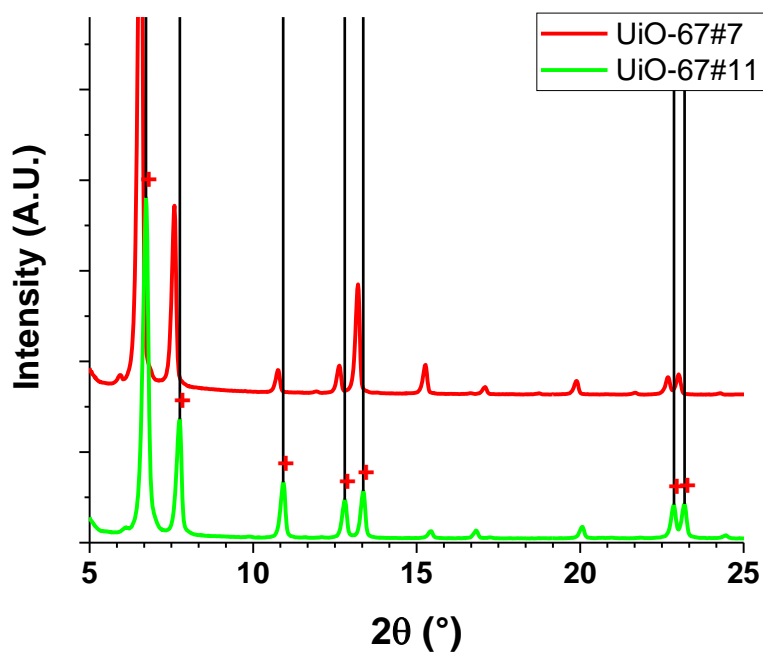

Figure 16: XRD results of UiO-67#7 (red) which was synthesised with 30eq AA and of UiO-67#11 (green) synthesised with 30eq BA.

The ATR-FTIR data in Figure 18 is labelled with the vibrations and stretches that have been found in literature as shown in

. The UiO-67#12 that was synthesised with AA at 120°C has sharper peaks than UiO-67#11 synthesised with BA. This indicates a purer and more uniform crystal structure. The SEM images in Figure 17 also supports this claim as we see crystals in more different sizes in the right sample that was synthesized with BA. Furthermore the physisorption results that were shown in Table 6 show that the UiO-67#11 synthesised with BA has a lower mesoporosity (3.53%) than UiO-67#7 (9.01%) and UiO-67#12(36.15) that were synthesised with AA under the same conditions. So AA was chosen because mesopores are reported to be beneficial for catalytic activity.

The difference between UiO-67#7 and UiO-67#12 is indicative of the difficulty to reliably create the exact same MOF structure because they had the same reaction conditions. However UiO-67#7 has less sharp ATR-FTIR peaks and broader XRD peaks hinting at a different crystallinity and this is also the reason why the Ar-physisorption results differ so much.
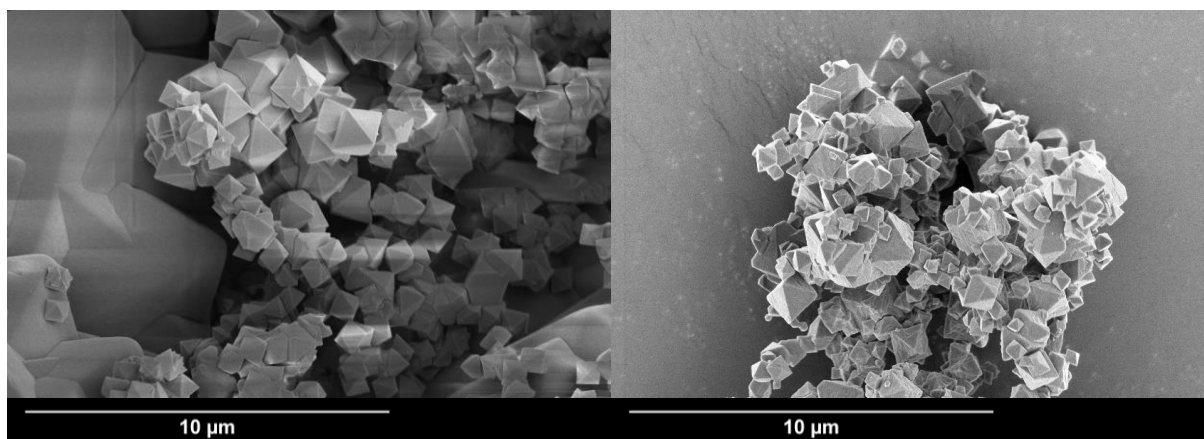

Figure 17:SEM images of UiO-67#7 (30eq AA) on the left and UiO-67#11 (30eq BA) on the right.

Table 7: FTIR peak positions and corresponding vibrations of stretching of chemical groups.

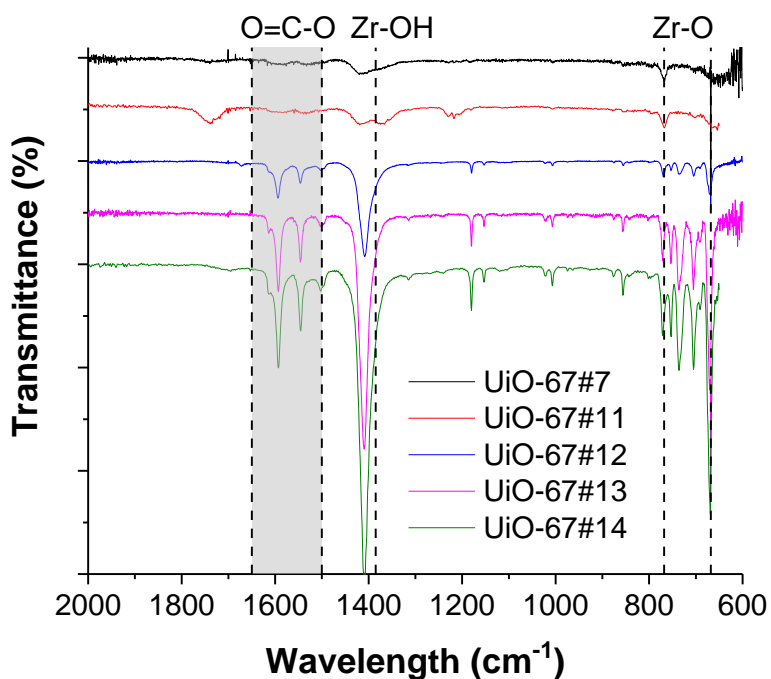| Peak position (cm⁻¹)	Chemical cause	Ref
668	Longitudinal vibrations Zr-O	[66],[67],[65]
768	Transvers vibrations Zr-O	[66],[67],[65]
1300-1400	Zr-OH	[65]
1385	Zr-OH	[66],[65]
1400-1600	O-C=O stretching from carboxylate group of bpdc linker	[67],[68]
1500-1650	C-O-Zr	[66]
2500-3300	O-H stretching from a carboxylic acid group	

Figure 18: ATR-FTIR data from UiO-67 synthesised with 30eq AA (black and red) and 30eq BA (blue) at 120C. And at 100C with 30eq AA (pink and green) .
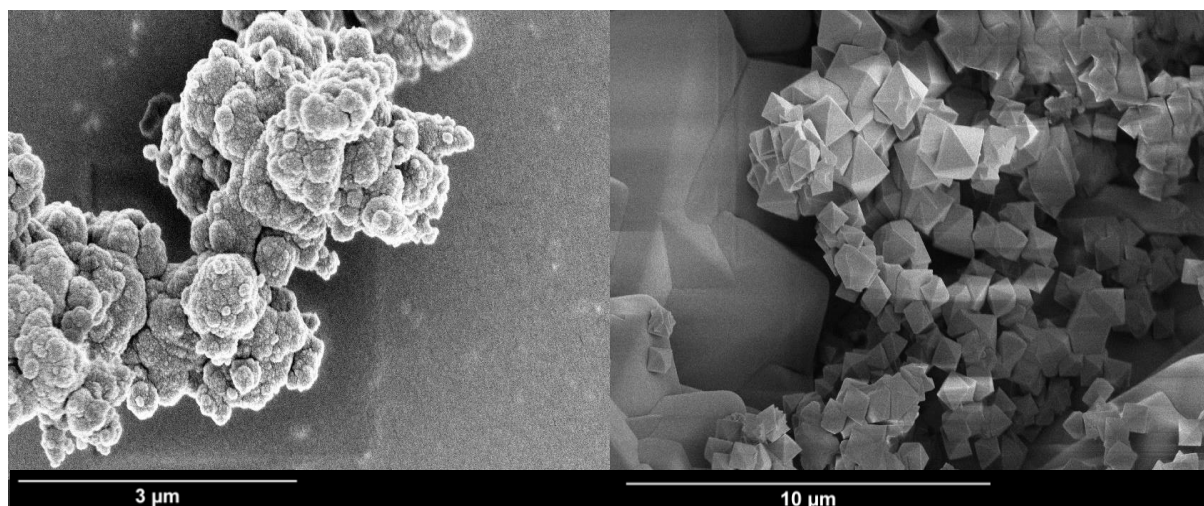
Figure 19: SEM images of UiO-67#5 synthesised with 1eq AA (left) and UiO-67#7 synthesised with 30eq AA (right)

The amount of modulator has a great impact on the crystalline structure as can be seen in the XRD data in Figure 20. The peaks get sharper as the amount of modulator increases which is in accordance with literature. The synthesis done with 1eq AA and 10eq AA are so amorph that there were no pores found with Ar-physisorption as can be seen in Table 6. The SEM images in Figure 19 also show that with 1eq AA only amorph structures are present while with 30eq AA there are very crystalline UiO-67 octahedral shaped crystals.
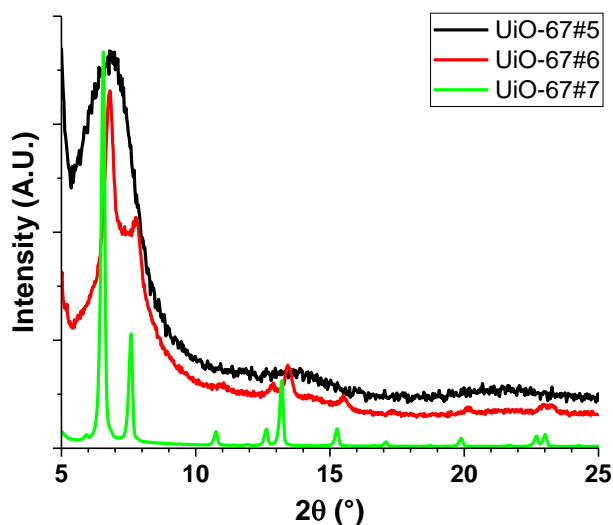

Figure 20: XRD data of UiO-67 synthesised with 1 (black) , 10 (red) and 30eq (green) AA.

2. Effect of temperature

In Figure 18 FTIR data of UiO-67#13 and #14 show much sharper peaks, this is even better visible in figure A2 that shows the zoomed in FTIR data of 600-800cm^{-1} where the two peaks of Zr-O vibrations are clearly visible. These two reactions were done at 100°C which is below the boiling point of AA at 118°C. By lowering the reaction temperature from 120°C (as is often used in literature) to 100°C the AA does not boil and the reaction becomes more reproductible and forms a structure with better purity and crystallinity. This better reproducibility can be seen when looking at the BET surface area of these two samples which are 3162 and 3243 m^2/g. However the difference in mesoporosity is still big so the reproducibility can still be increased.

When comparing the SEM images in Figure 19 with the ones in

Figure 21 it is visible that at 100°C the crystal size is smaller and the size distribution is not as broad. So at a lower temperature there is more precise control over the crystal size. Furthermore the physisorption results of these synthesis also show a bigger surface area and increased mesoporosity of 3162 and 3243m^2/g and 9.96% and 25.32% which are both beneficial for a good catalyst.
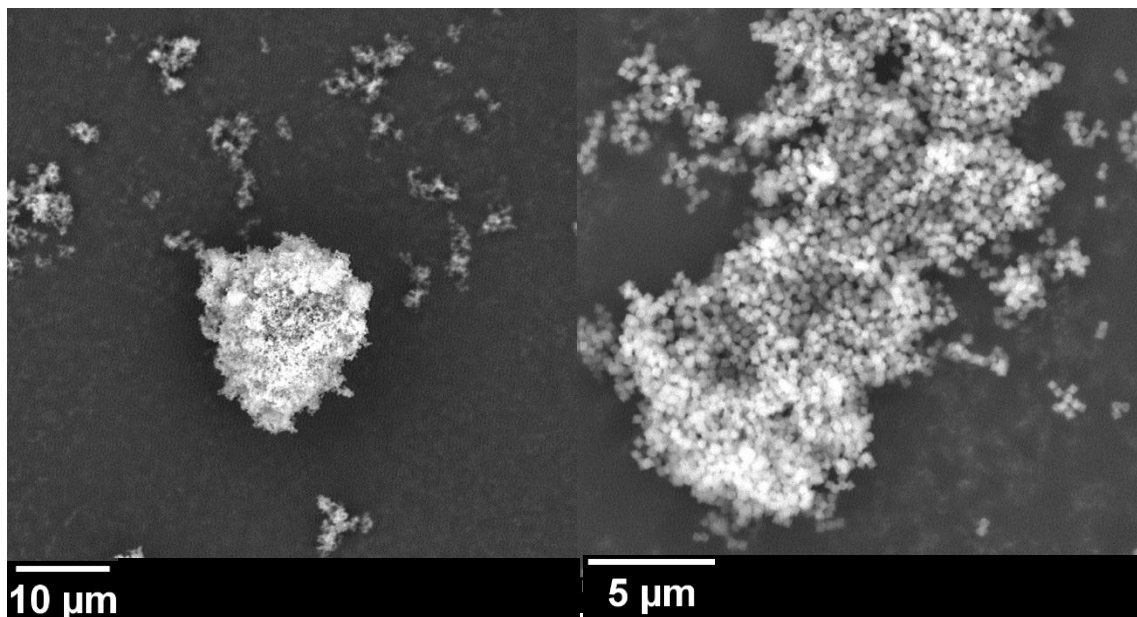

Figure 21:SEM images of UiO-67#13 on the left and UiO-67#14 on the right which are both synthesised at 100°C.

3. Round bottom flask synthesis

When looking at the XRD data in Figure 23 the synthesis done in a roundbottomflask with stirring for 24 hours (UiO-67#9) is very similar to the normal autoclave procedure (UiO-67#12). However the one that was synthesised for 48 hours in a roundbottomflask with stirring (UiO-67#10) shows some new peaks at 11.9, 14.8, 19.9 and 22.3° 2θ which are shown as a line without a red + in the graph. Indicating new crystal lattices formed. The SEM images in Figure 22 also confirm this because in the picture of UiO-67#10 there are no typical octahedral crystals visible but flat platelets. These platelets have a small BET surface area of 1367 m2/g so they have not been catalytically tested. As far as our knowledge this is a new structure. Hexagonal nanosheets have been reported by Firth et al. [69] when grinding their UiO-67 crystals, however our nanosheets are rectangular instead of hexagonal.
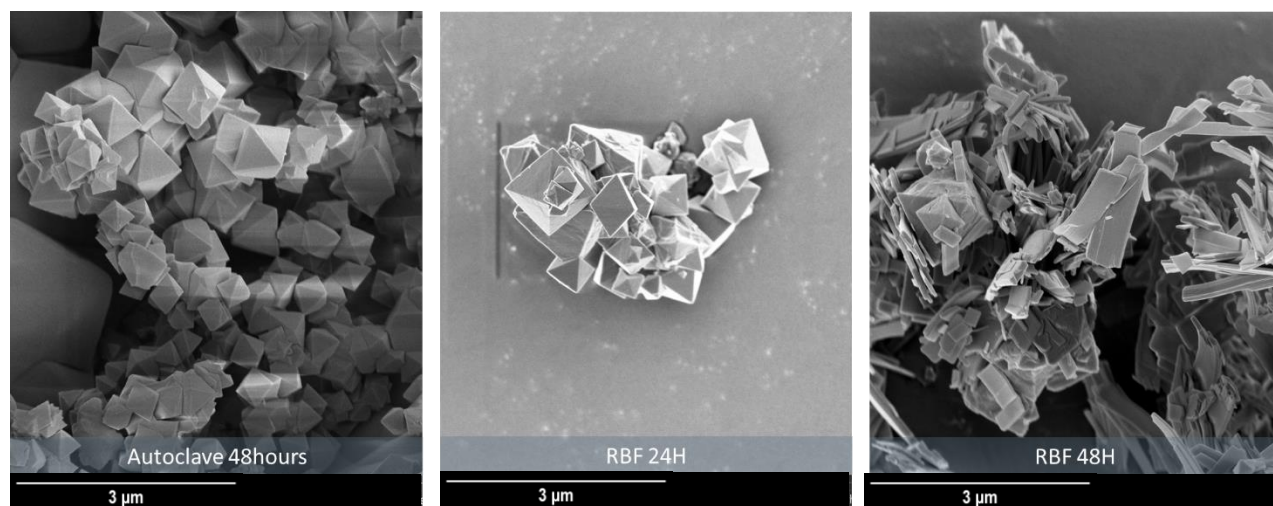

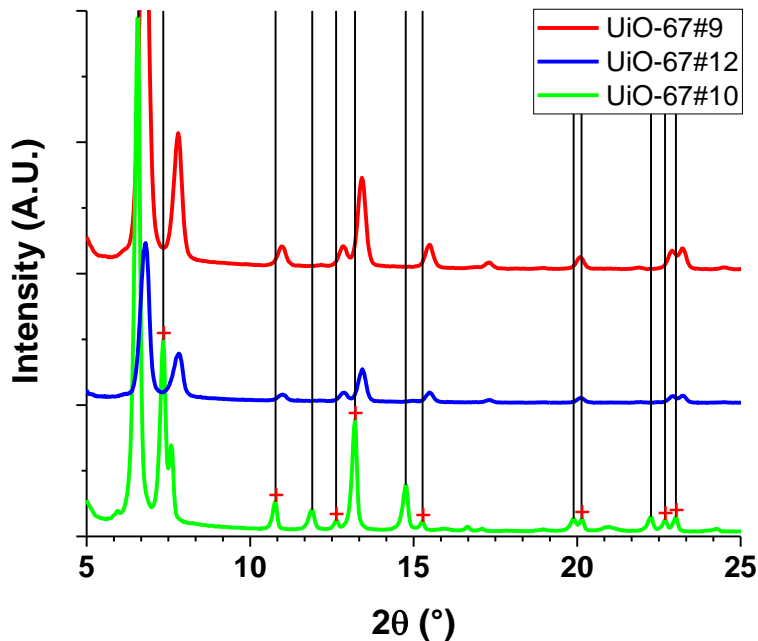*Figure 22: SEM images of UiO-67#12,9, and 12 from left to right*

Figure 23: XRD data of UiO-67 synthesised in a roundbottomflask with stirring for 24h (red) 48h (green) and the normal synthesis procedure in an autoclave (blue)

4. Sample spin coating

To find the best way of spin coating the UiO-67 ethanol and toluene were tried as solvents. Ethanol has been previously reported as a good solvent for spin coating a uniform layer of UiO-67 [70]. However ethanol is an alcohol and will deteriorate the perovskites so a replacement must be found. The perovskite quantum dot solutions are suspended in toluene so if toluene could also work for spin coating UiO-67 it would be ideal.

In Figure A4 the SEM images of the two different results are shown and toluene shows an even better surface coverage and uniform layer than ethanol. So toluene can be used to spin coat the UiO-67 layers on the borosilicate wafer.

In Figure 24 the ATR-FTIR spectra are shown of UiO-67 spin coated on wafers. The clean wafer has multiple peaks between 800 and 1400 cm-1 that are not visible after UiO-67 is spin coated on top of the wafer. This is because ATR-FTIR is a surface sensible technique so when the UiO-67 layer is thick enough it will not penetrate to the borosilicate wafer [71]. The characteristic peaks for UiO-67 for Zr-OH and O=C-O are visible for the fresh samples however they become way

more sharp after photocatalysis. This indicates a more pure sample where remaining toluene and amorph material is flushed away during the reaction. The UiO-67 crystals seem to remain stable during photocatalysis when looking at the ATR-FTIR data.
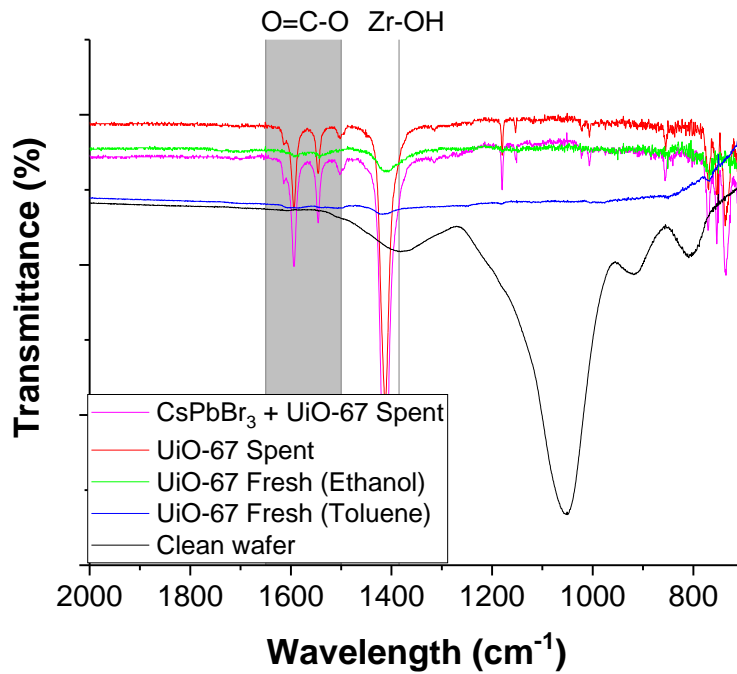

Figure 24: ATR-FTIR data of spin coated samples on a borosilicate wafer. The spent catalysts were analysed after the photocatalytic testing.

ii. CsPbBr₃
1. Effect of temperature

The particle size of the $CsPbBr_3$ crystals were determined by an analysis with ImageJ software of the TEM images shown in Figure 26. The synthesis at 150°C resulted in bigger crystals on average (17.61 ± 5.00nm) but with a high particle size distribution. While the $CsPbBr_3$#1 and $CsPbBr_3$#2 synthesised at 130°C were smaller (11.06 ± 3.12nm, 7.17 ± 1.17nm)) and with a narrower particle size distribution. The broad particle size of $CsPbBr_3$#3 is due to the formation of nanoplatelets in addition to the square nanocrystals seen. In Figure 26d the more nonhomogeneous nanoplatelets are shown as a cluster in the centre and on the top left the nano cubes are visible. These platelets have been seen before at lower reaction temperatures of 90°C and 130°C [72].

In the TEM image for $CsPbBr_3$#1 there are also hexagonal crystals visible next to the cubical crystals. These were also synthesised by Zhong et al. [73] at a reaction temperature of 90°C. They concluded that the ligands absorbed on the edges of a hexagonal crystal became unstable at

higher temperatures. So they reaction conditions might have not been totally homogenous as multiple crystal structures formed.
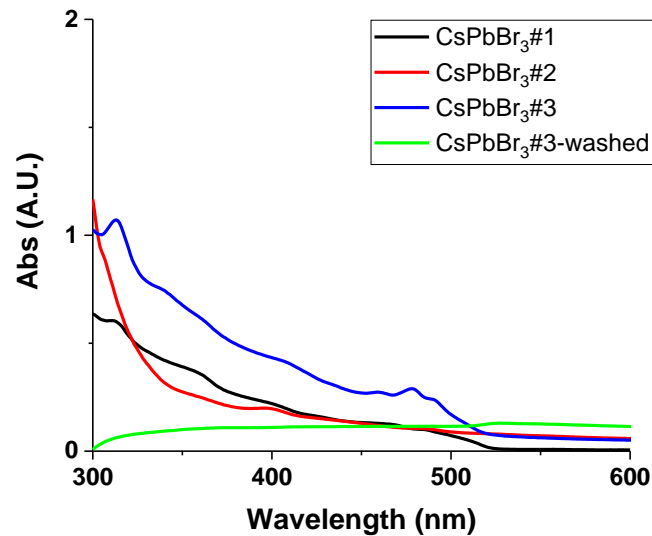
Figure 25: UV-vis results of CsPbBr₃.

When looking at the UV-vis results in Figure 25 the $CsPbBr_3$#3 shows the best absorption at 600-300nm with two distinct peaks at 312 and 480nm. The peak at 480 can be described to $CsPbBr_3$ square nanocrystals [74], however the peak at 312 is from $CsPb_2Br_5$ [75]. The UV-vis spectra from $CsPbBr_3$#3 is very similar to the UV-vis spectrum of $CsPb_2Br_5$ micro sheets found by Tang et al. [76].

Sheets have a similar bandgap and also good optical properties so should also be a good photocatalyst.
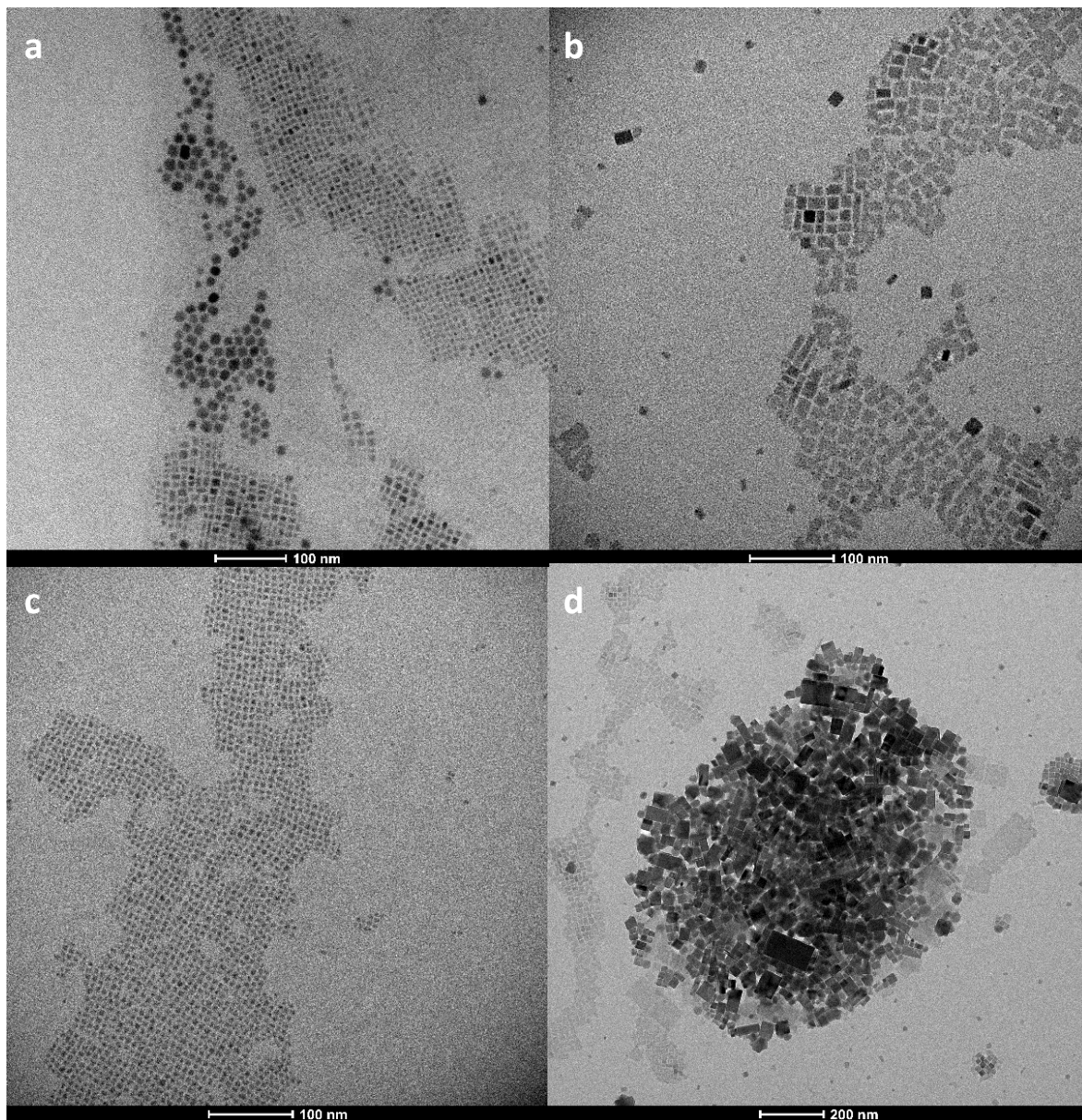
Figure 26: TEM images of CsPbBr3 #1 (a), #2 (b) synthesised at 130°C and CsPbBr3#3 synthesised at 150°C (c and d).

CsPbBr$_3$#3 was chosen for catalytic testing because of the best photon absorption and the combination of nano cubes and nanoplatelets. The nanocubes have a smaller bandgap which is good for photo absorption while the platelets have a bigger bandgap [72] which is good for the redox capability. If there is electron transport possible between the two phases it could be a potential impressive Z-type photocatalyst.

2. Spent catalyst

The peaks at 15.2 and 30.5° 2θ in Figure 27 correspond to the {100} and {111} crystal planes that are present in an orthorhombic phase of $CsPbBr_3$ [77][26]. The spent catalyst has a new peak at 11.7° 2θ which is a peak indicative of the {002} crystal lattice of the tetragonal phase of $CsPb_2Br_5$ [78]. The pure $CsPb_2Br_5$ phase has shown to have lower photocatalytic conversion of CO_2 however a specific combination of $CsPb_2Br_5$ with $CsPbBr_3$ can form a direct Z-scheme and this increased the photocatalytic activity [75]. In our case it will most likely reduces the catalytic activity over time.
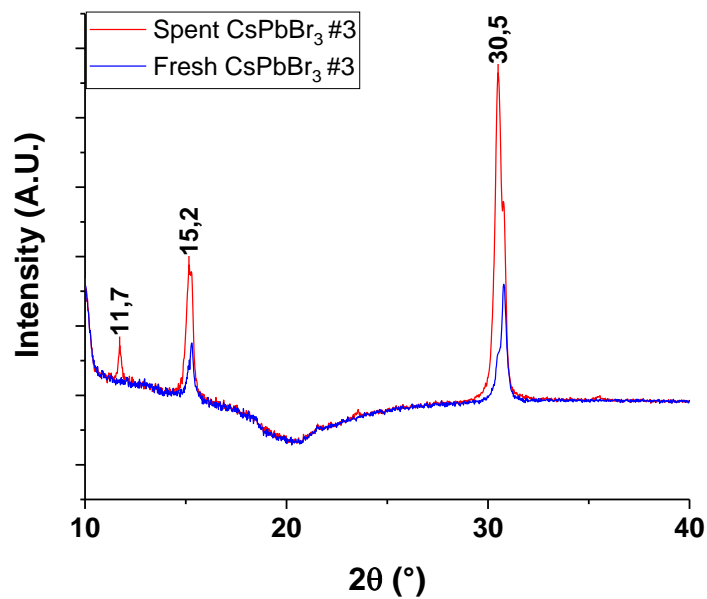
Figure 27:XRD of CsPbBr₃ before and after photocatalysis

The ATR-FTIR results in Figure 28 show the positions of the CH_3 stretch, CO bending and CH bending in the oleic acid and oleylamine ligands [20]. In the fresh sample (blue line) the organic ligands are clearly visible in the IR spectrum. After catalysis the peaks disappear when analysing the spent sample. This indicates the ligands are flushed off or reacting with the CO_2 and H_2 during the photocatalytic reaction. The double inverse peak visible at the spectrum of the clean wafer at 2400cm^{-1} is an indication of a change in CO_2 concentration in the atmosphere between the background measurement and the measurement of the wafer so it is not significant. In the IR results of the $CsPbBr_3$ spin coated sample the peaks from the borosilicate wafer are still visible in the spectrum. This indicates that the layer is less thick than the UiO-67 coated sample. When looking at the sample of UiO-67 spin coated over $CsPbBr_3$ (green line) only the UiO-67 peaks are visible and not the wafer or ligand peaks. So this suggests pretty good coverage of the $CsPbBr_3$ layer. When looking at the SEM image of the $CsPbBr_3$ wafer in Figure A3 there are two

phases visible and it looks like there is less coverage than in the UiO-67 coated wafers. The two phases could be a layer of quantum crystals with a bit of bulk $CsPbBr_3$ on top.
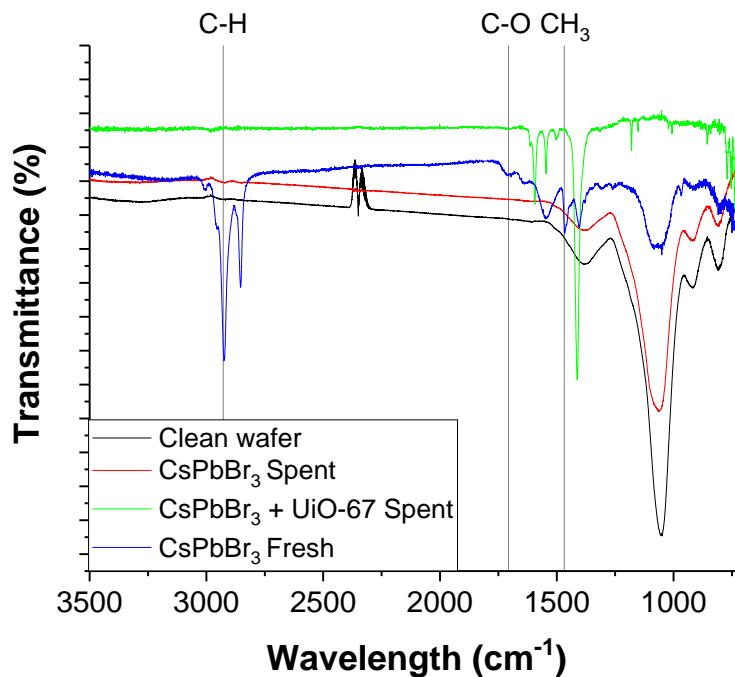
Figure 28: ATR-FTIR results of CsPbBr₃. The spent catalysts were analysed after the photocatalytic testing.

iii. Cs₂AgBiBr₆
1. Effect of reaction time

The CABB crystal sizes were also analysed by ImageJ software and CABB#1 with a reaction time of 15s has a crystal size of 10.09 ± 1.36 and the CABB#2 with a reaction time of 10 seconds has a crystal size of 8.87 ± 1.33. Both have a narrow crystal size distribution indicating a good homogenous synthesis method. There are also some dense darker crystals visible on the TEM images in Figure 30 which could be a different phase such as AgBr crystals.
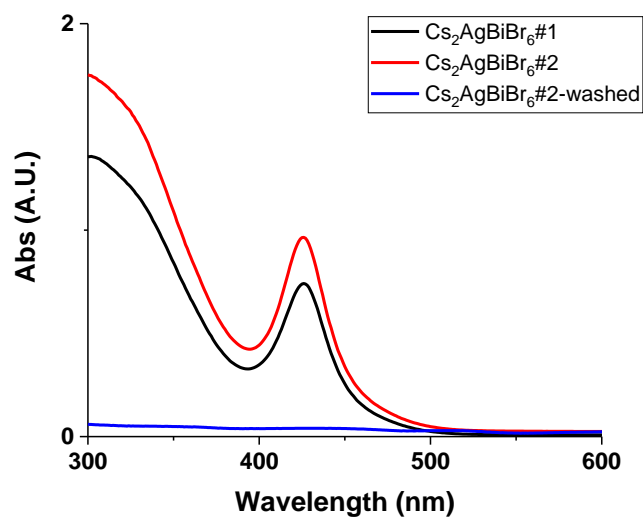
Figure 29:UV-vis results of CABB

The absorption spectra are very similar and the only difference is that CABB#2 has a bit higher absorption which indicates a bit higher concentration, so this batch was used to spin coat the samples that were used for catalytic testing.
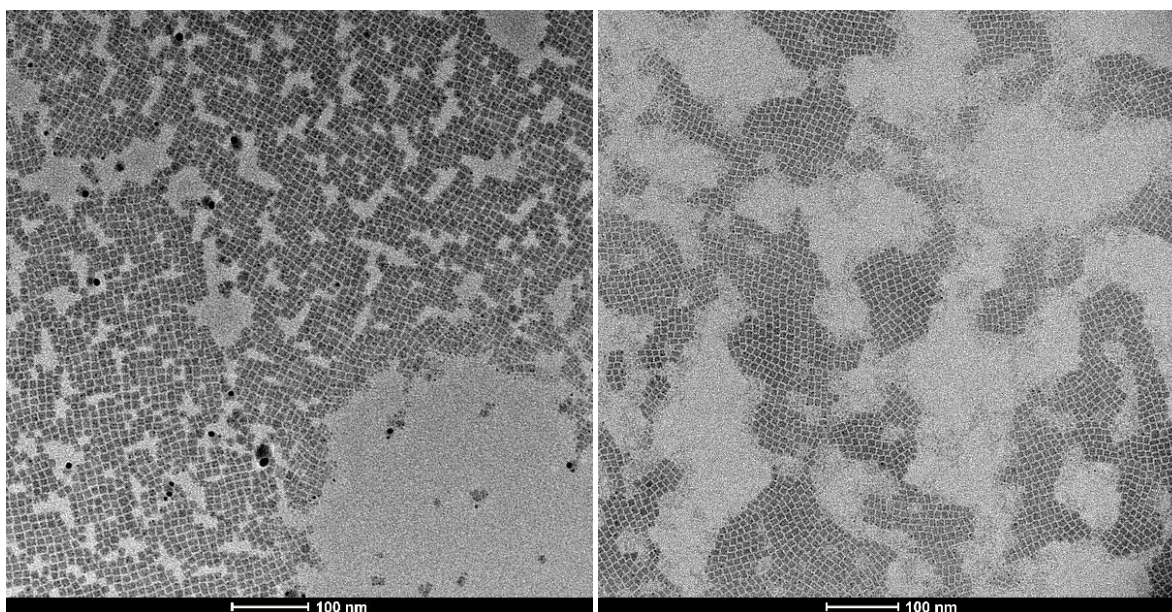
Figure 30: TEM images of CABB#1 (left) and CABB#2 (right)

2. Spent catalyst

The IR peaks for the organic ligands are abundantly present in the drop casted sample (cyan line) and present in a small amount in the spin coated sample (green). This is because the drop casted sample has more grams of perovskite on the wafer so there will also be more ligands present. After the spin coated sample is used for photocatalytic testing with and without added water the peaks disappear (blue and red) so the ligands are flushed away during testing. This can have a positive effect on the photocatalytic activity as is shown by Zhou et al. [79] because the perovskite is better accessible for CO_2.
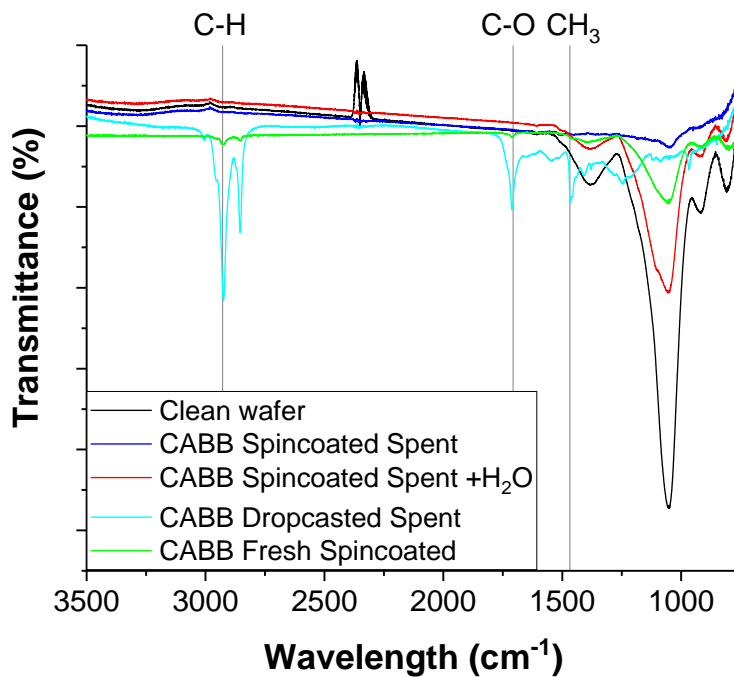
Figure 31: ATR-FTIR spectra of CABB wafer samples. The spent catalysts were analysed after the photocatalytic testing.
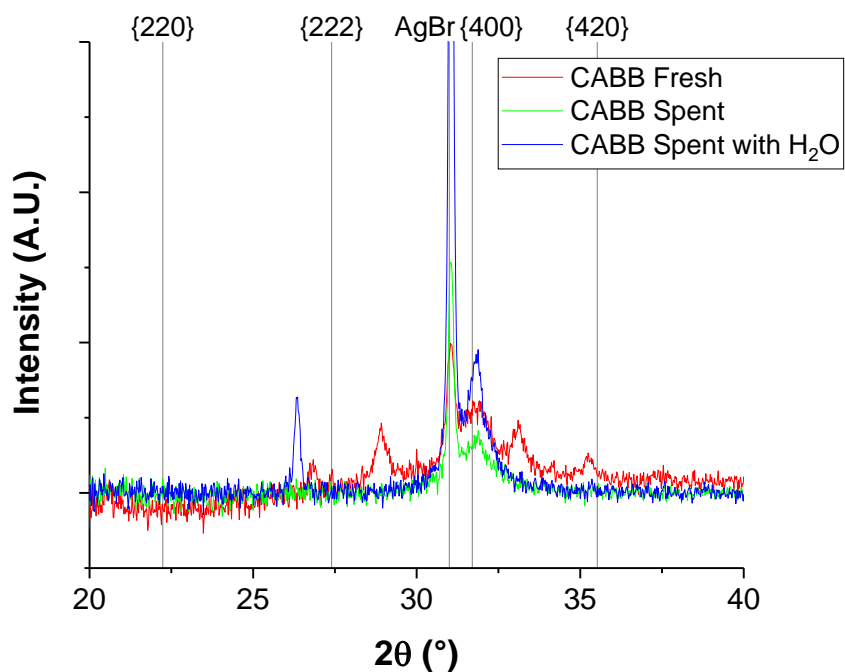
Figure 32: XRD results of spin coated CABB.

The XRD results show a peak at crystal phase {400} [80,81] for the spin coated sample. This peak is enhanced in contrast to the peaks of phase {220}, {220} and {420} because of the orientation alignment of CABB on the borosilicate wafer[36]. The peak next to it is a side phase AgBr [82]. Which was shown to be present when an annealing step that is lower than 250°C was used after spin coating. A annealing step of 120°C was used in our method so some AgBr is expected. However when looking at the spent catalysts the AgBr increases in intensity compared to the {400} CABB peak. This suggests that during photocatalysis the CABB deteriorates into AgBr.

b- Photocatalytic testing
i.   Conversion

First the gas chromatography (GC) results of the photocatalytic tests will be analysed by looking at the total CO_2 conversion. All samples have some initial CO_2 conversion ranging from 0.7 to 2.7 mmol/s as can be seen summarised in Table 8. This activity is a lot higher than reported in literature for these catalysts which is around 0.036mmol/s with our catalyst loading. However this activity is already present when the light is not even turned on and decreases quickly as can be seen in Figure 33. So this initial conversion cannot be photocatalytic activity but is probably to the effect of the reaction cell needing quite a lot of time to be totally saturated with CO_2 so it

is hard to calibrate at the start of the reaction. This is because the cell is square and the flow is only through the middle so it will take more time to flush the outer corners as well with CO_2. Another possibility is that the organic ligands or toluene that is used for spin coating first reacts with H_2 and CO_2 however this is unlikely because the same trend is observed in the blanco measurement without catalyst.

The blank measurement done with a clean borosilicate wafer also shows that the CO_2 conversion is very unstable to measure in the GC with such quantities. So it is hard to say anything quantitatively about the samples however we can still get some qualitative conclusion when looking at the GC peaks. To get quantitatively reliable results there should be more conversion. A batch reactor with offline GC would be more suited however that equipment was not available during this research.

Table 8: Summary of CO_2 conversion results

Sample	Light	CO_2 conversion (%)	CO_2 conversion (mmol/s)	Deactivation to 0%
$CsPbBr_3$	off	4.5	2.7	20 minutes
$Cs_2AgBiBr_6$	off	2.5	1.5	20 minutes
UiO-67	off	3.2	1.9	16 minutes
$CsPbBr_3$	on	0.7	0.4	8 minutes
$CsPbBr_3$ + UiO-67	on	3.5	2.1	12 minutes
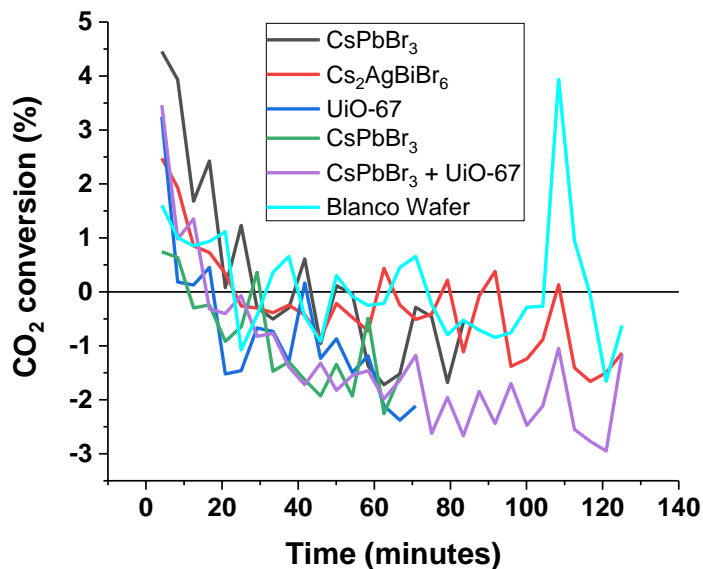
Figure 33: CO₂ conversion results of all samples

During photocatalytic testing there was an unknown peak that came before the CO peak. It could not be H_2O, N_2 or Kr as these gasses are not combusted by our FID detector so it has to be something with C atoms. The CO and CO_2 are methanized and therefore visible with the FID detector. Other products such as methanol or ethene would have a higher retention time than CO so it is unclear what this peak could be. Side products such as formic acid or formaldehyde have low sensitivity for the FID so are also unlikely. So for the analysis here we will call this product Y. The GC results of the blanco measurement also showed this product Y formation however at a constant low rate as is seen in Figure A6.

The setup was tested with a spin coated TiO_2 sample and this sample was found to be photo catalytically active for the reduction of CO_2 into CO. This can be seen in the left graph in Figure A5 by the CO that was only formed after the light was turned on. So we know our setup is able to show photocatalytic activity even if the yield is very low.

ii.   Comparing perovskites CsPbBr$_3$ with Cs$_2$AgBiBr$_6$
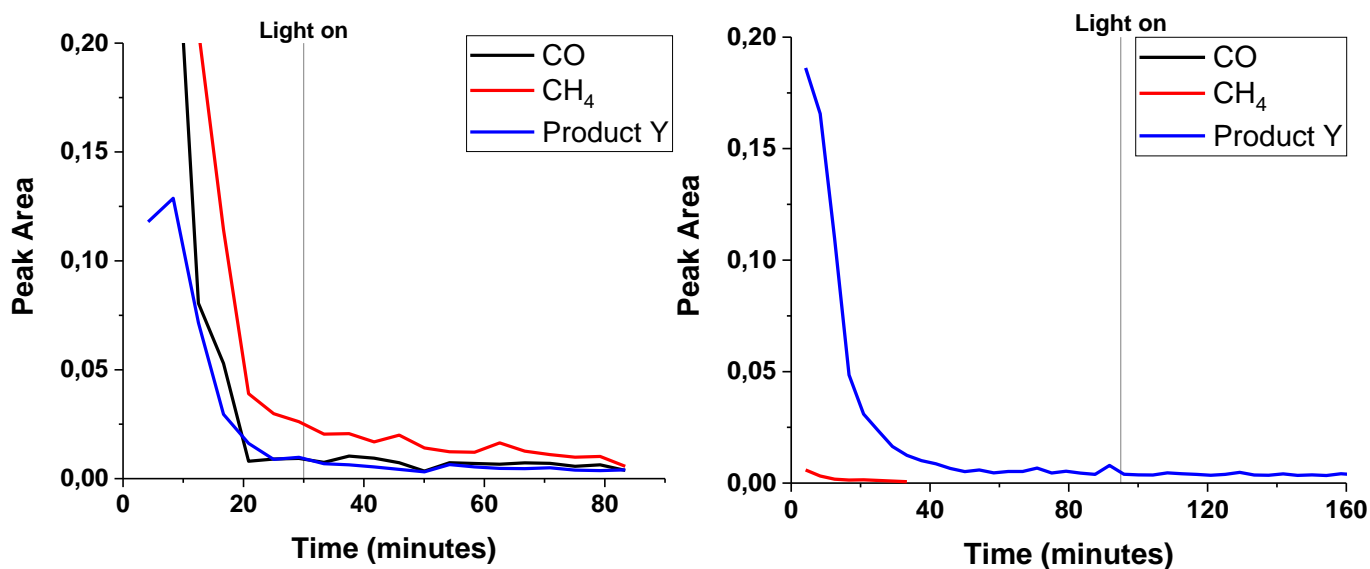
Figure 34: GC results of CsPbBr$_3$ (left) and CABB (right)

When looking at Figure 34 it is visible that CsPbBr$_3$ (left) has bigger product peaks for CH$_4$ and CO at the start and over time. However it is hard to tell if this is due to photocatalytic effect because it is already formed before the light is turned on and after the light is turned on there is no significant change in the trends. For CABB on the right more product Y is formed but barely any CH$_4$ and no CO. This doesn't change when the light is turned on. This indicates that CABB is not photo catalytically active under these circumstances but CsPbBr$_3$ might be. This can be explained by the low CO$_2$ adsorption efficiency of perovskites which makes it harder to convert CO$_2$ in this solid-gas method than in the solid-liquid mode where CABB has proven to work as a photocatalyst.

However in a second test with the same CsPbBr$_3$ the results were very different. In Figure 35 on the left this results can be seen. In this test the light was turned on during the N$_2$ flushing and after 30 minutes the CO$_2$ and H$_2$ flow was turned on. This resulted in an initial formation of Product Y and a tiny bit of CH$_4$ before it started deactivating. This is similar to the previous results of the CABB sample. This begs the question what is happening with the CsPbBr$_3$ sample during catalysis. In IR and XRD there was no difference in both spent samples. So a possible explanation would be a contamination during the first measurement which showed high conversion at the start.
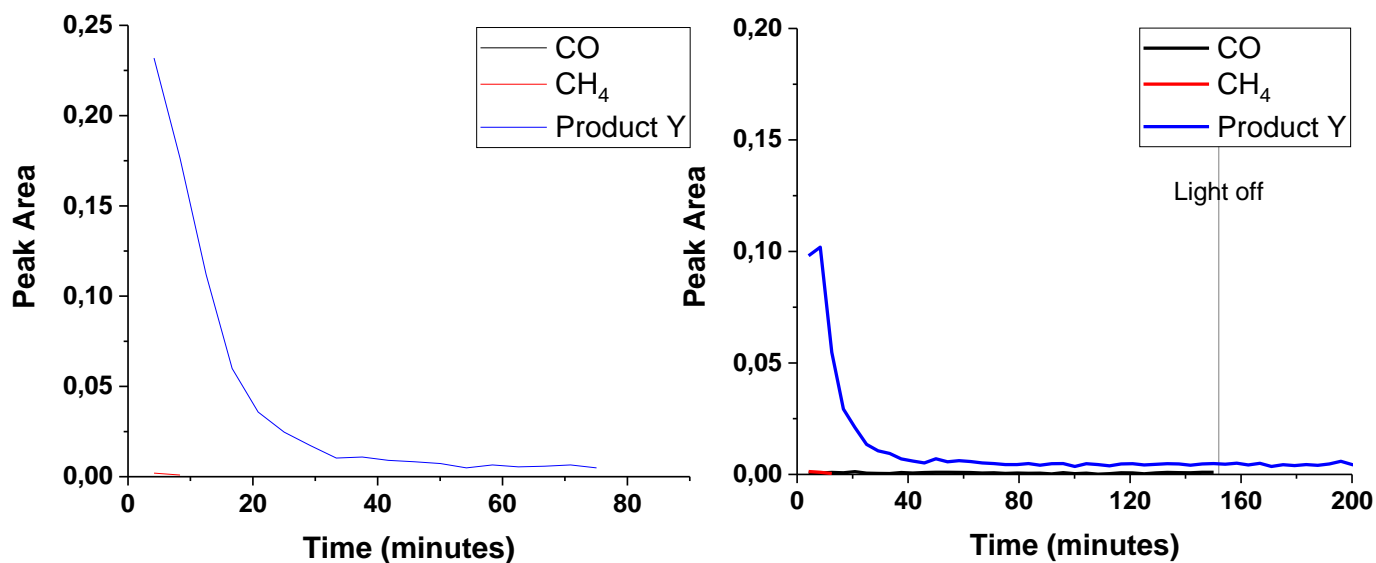
Figure 35: GC results of CsPbBr₃ (left) and CsPbBr₃ + UiO-67 (right)

iii.   Effect of adding UiO-67

First we will look at the photocatalytic activity of pure UiO-67 which is shown in Figure 36 (right). There is again initial formation of product Y and CH_4 which slowly deteriorates after time and the moment the light is turned on there is no change in trends. This suggests UiO-67 on its own is not photo catalytically active under these circumstances. However when we look at the graph on the left in the same figure we can see the results of the sample with a combination of $CsPbBr_3$ and UiO-67. This is the first time we undoubtedly see a photocatalytic active sample for CO formation besides the TiO_2. This is because when the light is on there is CO and product Y formation but when the light is turned off after 2.5 hour the CO peak disappears. So product Y is not photo catalytically formed but CO is.

The combination of $CsPbBr_3$ and UiO-67 resulted in photocatalytic activity where there was none with the individual components. This can be explained by the fact that the combination of UiO-67 and $CsPbBr_3$ has a chance of forming a Z-scheme which improves the carrier separation and redox capability at the surface. Furthermore the UiO-67 has excellent CO_2 adsorption so there will be more immobilised CO_2 in close contact with the perovskite to react with the electrons.
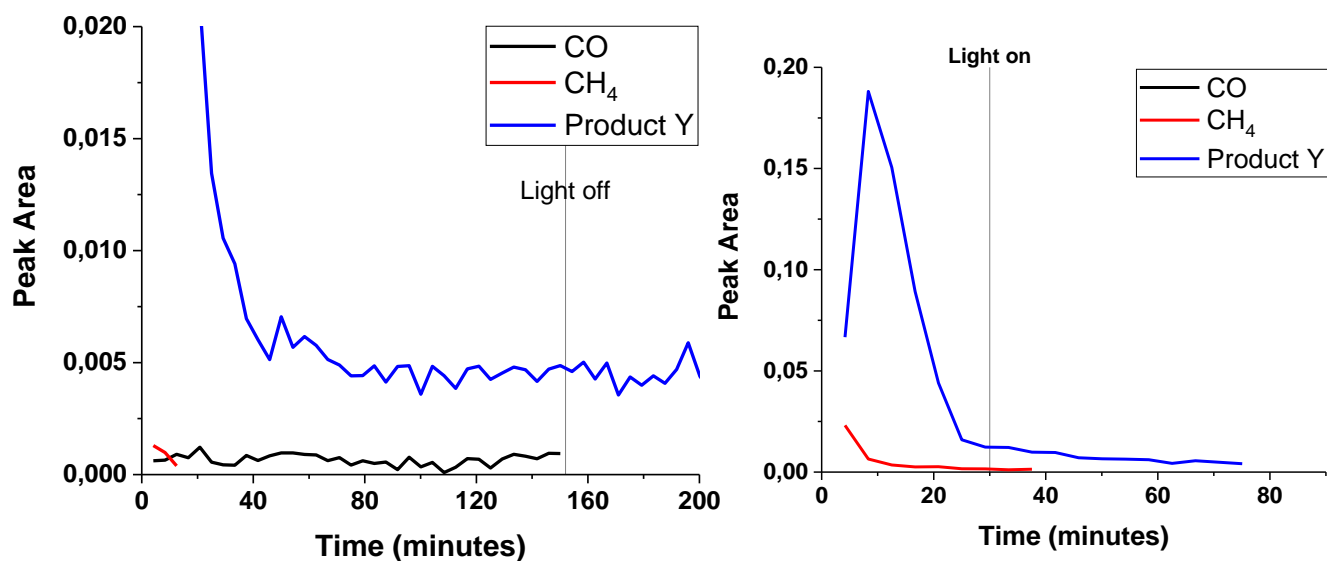
Figure 36: GC results of CsPbBr₃ + UiO-67 (left) and UiO-67 (right)

iv.   Effect of adding H_2O

For CABB two tests were done, one without a H_2O bubbler which is shown in the left graph and one with an added bubbler which is shown in the right graph of Figure 37. When testing with only CO_2 and H_2O there were no products seen at all. However when the H_2 flow was turned on as well there was the initial high product Y formation and a steady CO formation. This CO formation could be photocatalytic activity as the light is on the entire time. So when adding a H_2O bubbler and still flowing H_2 there is CO formed while this is not the case for CABB with only H_2.

To the best of our knowledge this is the first time CABB has been shown to be active in the solid-gas phase for CO_2 reduction. However it is only active when a combination of H_2O vapour and H_2 is used. When comparing this to the test done with TiO_2 and a H_2O bubbler which is shown on the right in Figure A5 it looks very similar. The TiO_2 does not have any product formation when only H_2O is turned on but does have CO formation when H_2 is added.
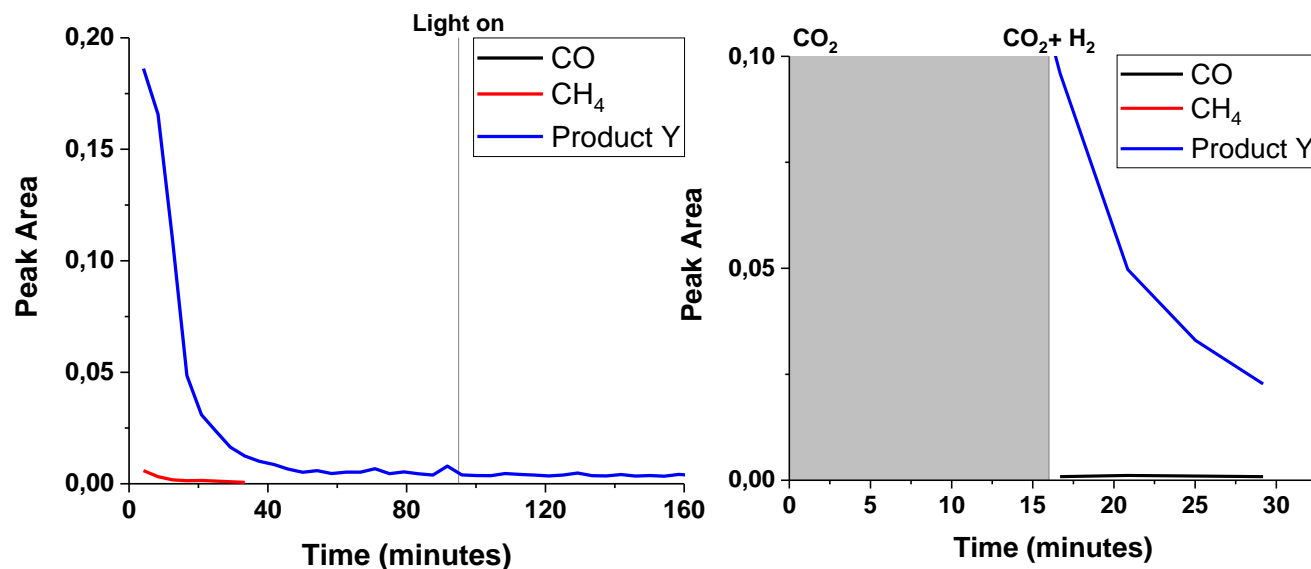
Figure 37: GC results of CABB with (right) and without (left) added H_2O

4. Conclusions and outlook

UiO-67

For the synthesis of UiO-67 a method with 30 eq acetic acid at 100°C was deemed the best because it gave a crystalline MOF with the highest BET surface area and good mesoporosity. Since acetic acid is used as a modulator in the synthesis, it is advised to keep the synthesis temperature below its boiling point.

UiO-67 on itself is not photo catalytically active for CO_2 reduction under the circumstances tested but it does activate the CABB which is unactive on its own in a H_2 stream. So to conclude UiO-67 is still a very promising candidate for enhancing perovskite activity and stabilising the catalyst. Further research should be done on the stability and reactivity in aqueous media instead of a solid-gas phase.

Replacing CsPbBr$_3$

CsPbBr$_3$ has shown to be unreliable due to non-repetitive results. therefore more experiments are needed in order to prove if the sample is photo catalytically active under the given circumstances. The CsPbBr$_3$ has shown to become active when combined with UiO-67.

CABB was not found to be photo catalytically active in its pure form with a CO_2 and H_2 gas flow. However when H_2O was added to the reaction there was photocatalytic reduction of CO_2 to CO.

$CsPbBr_3$ should also be checked with added H_2O and CABB with UiO-67 to see if CABB really is a notable replacement for $CsPbBr_3$. The photocatalytic conversion of CO_2 to CO by CABB has not yet before been achieved in a solid-gas method but is confirmed by these results.

Combination

When perovskites were combined with UiO-67 very promising results were attained, however further experiments are still needed . In this study a heterojunction of two layers was formed but other synthesis methods should be explored to see if the perovskite could be grown inside the UiO-67 pores to have even more interaction and therefore effect on stability and activity.

To check if a Z-scheme is really formed electronic calculation could be done on the valence and conduction band.

The addition of water to a H_2 stream did activate CABB so has shown to be of added value to the photocatalytic mechanism. However H_2O on its own did not accommodate photo catalytic activity on CABB and TiO_2.

For $CsPbBr_3$ testing with H_2O should also be tried to see if it also results in unambiguous photocatalytic activity.

Finally, the most from the previously described results, a repetition is needed in a batch or circular reactor so the product can accumulate over time and be at a high enough concentration to be analysed quantitatively by a GC. This way we can not only see if the sample is photo catalytically active but also compare the yields. However these continuous testing have shown that most of the activity is at the start of the reaction even when the light is off. So this is something to keep in mind when doing a batch reaction where you can't see the results over time.

Furthermore the results should be compared to a testing setup with a solid-liquid method to compare those two methods and see which one has more potential. If the solid-liquid method could be performed in water because of the stable UiO-67 or a higher percentage of water in ethyl acetate which could increase photocatalytic active because water is used to form H^+ and *H to activate the CO_2.

A GC-MS measurement needs to be carried out to find out what product Y is.

5. Acknowledgements

References

1. Concepcion, J. J., House, R. L., Papanikolas, J. M. & Meyer, T. J. Chemical approaches to artificial photosynthesis. *Proc. Natl. Acad. Sci. U. S. A.* **109**, 15560–15564 (2012).

2. Xie, S., Zhang, Q., Liu, G. & Wang, Y. Photocatalytic and photoelectrocatalytic reduction of CO2 using heterogeneous catalysts with controlled nanostructures. *Chem. Commun.* **52**, 35–59 (2016).

3. Fujishima, A. & Honda, K. Electrochemical photolysis of water at a semiconductor electrode. *Nature* **238**, 37–38 (1972).

4. Inoue, T., Fujishima, A., Konishi, S. & Honda, K. Photoelectrocatalytic reduction of carbon dioxide in aqueous suspensions of semiconductor powders [3]. *Nature* **277**, 637–638 (1979).

5. Ola, O. & Maroto-Valer, M. M. Review of material design and reactor engineering on TiO2 photocatalysis for CO2 reduction. *Journal of Photochemistry and Photobiology C: Photochemistry Reviews* **24**, 16–42 (2015).

6. Luo, J. *et al.* Halide perovskite composites for photocatalysis: A mini review. *EcoMat* **3**, (2021).

7. Anpo, M., Yamashita, H., Ichihashi, Y. & Ehara, S. Photocatalytic reduction of CO2 with H2O on various titanium oxide catalysts. *J. Electroanal. Chem.* **396**, 21–26 (1995).

8. Abdullah, H., Khan, M. M. R., Ong, H. R. & Yaakob, Z. Modified TiO2 photocatalyst for CO2 photocatalytic reduction: An overview. *Journal of CO2 Utilization* **22**, 15–32 (2017).

9. Lo, C. C., Hung, C. H., Yuan, C. S. & Wu, J. F. Photoreduction of carbon dioxide with H2 and H2O over TiO2 and ZrO2 in a circulated photocatalytic reactor. *Sol. Energy Mater. Sol. Cells* **91**, 1765–1774 (2007).

10. Wang, H. N. *et al.* Recent progress and perspectives in heterogeneous photocatalytic CO2 reduction through a solid–gas mode. *Coordination Chemistry Reviews* **438**, 213906 (2021).

11. Santomauro, F. G. *et al.* Localized holes and delocalized electrons in photoexcited inorganic perovskites: Watching each atomic actor by picosecond X-ray absorption spectroscopy. *Struct. Dyn.* **4**, (2017).

12. Zhang, Q. & Yin, Y. All-Inorganic Metal Halide Perovskite Nanocrystals: Opportunities and Challenges. *ACS Cent. Sci.* **4**, 668–679 (2018).

13. Jellicoe, T. C. *et al.* Synthesis and Optical Properties of Lead-Free Cesium Tin Halide Perovskite Nanocrystals. *J. Am. Chem. Soc.* **138**, 2941–2944 (2016).

14. Wu, Y. *et al.* Composite of CH3NH3PbI3 with Reduced Graphene Oxide as a Highly Efficient and Stable Visible-Light Photocatalyst for Hydrogen Evolution in Aqueous HI Solution. *Adv. Mater.* **30**, 1704342 (2018).

15. Zang, M., Zhao, C., Wang, Y. & Chen, S. A review of recent advances in catalytic combustion of VOCs on perovskite-type catalysts. *Journal of Saudi Chemical Society* **23**, 645–654 (2019).

16. Zhu, X. *et al.* Lead halide perovskites for photocatalytic organic synthesis. *Nat. Commun.* **10**, (2019).

17. Hou, J. *et al.* Inorganic Colloidal Perovskite Quantum Dots for Robust Solar CO2 Reduction. *Chem. - A Eur. J.* **23**, 9481–9485 (2017).

18. Xu, Y. F. *et al.* Enhanced Solar-Driven Gaseous CO2 Conversion by CsPbBr3 Nanocrystal/Pd Nanosheet Schottky-Junction Photocatalyst. *ACS Appl. Energy Mater.* **1**, 5083–5089 (2018).

19. Zhang, X., Tang, R., Li, F., Zheng, R. & Huang, J. Tailoring Inorganic Halide Perovskite Photocatalysts toward Carbon Dioxide Reduction. *Sol. RRL* 2101058 (2022). doi:10.1002/SOLR.202101058

20. Kaltzoglou, A. & Falaras, P. Recent developments on hybrid perovskite materials for solar energy conversion and environmental protection. *Current Opinion in Chemical Engineering* **33**, (2021).

21. Zhang, Z. *et al.* Artificial Photosynthesis over Metal Halide Perovskites: Achievements, Challenges, and Prospects. *J. Phys. Chem. Lett.* **12**, 5864–5870 (2021).

22. Wu, H. L., Li, X. B., Tung, C. H. & Wu, L. Z. Semiconductor Quantum Dots: An Emerging Candidate for CO2 Photoreduction. *Advanced Materials* **31**, 1900709 (2019).

23. Yui, T. *et al.* Photochemical reduction of CO2 using TiO2: Effects of organic adsorbates on TiO2 and deposition of Pd onto TiO2. *ACS Appl. Mater. Interfaces* **3**, 2594–2600 (2011).

24. Li, K., Peng, B. & Peng, T. Recent Advances in Heterogeneous Photocatalytic CO2 Conversion to Solar Fuels. *ACS Catal.* **6**, 7485–7527 (2016).

25. Kumar, N., Rani, J. & Kurchania, R. Advancement in CsPbBr3 inorganic perovskite solar cells: Fabrication, efficiency and stability. *Solar Energy* **221**, 197–205 (2021).

26. Wan, S., Ou, M., Zhong, Q. & Wang, X. Perovskite-type CsPbBr3 quantum dots/UiO-66(NH2) nanojunction as efficient visible-light-driven photocatalyst for CO2 reduction. *Chem. Eng. J.* **358**, 1287–1295 (2019).

27. Kong, Z. C. *et al.* Core@shell cspbbr3@zeolitic imidazole framework nanocomposite for efficient photocatalytic co2 reduction. *ACS Energy Lett.* **3**, 2656–2662 (2018).

28. Dong, Z., Zhang, Z., Jiang, Y., Chu, Y. & Xu, J. Embedding CsPbBr3 perovskite quantum dots into mesoporous TiO2 beads as an S-scheme heterojunction for CO2 photoreduction. *Chem. Eng. J.* **433**, 133762 (2022).

29. Zhou, L., Xu, Y. F., Chen, B. X., Kuang, D. Bin & Su, C. Y. Synthesis and Photocatalytic Application of Stable Lead-Free Cs2AgBiBr6 Perovskite Nanocrystals. *Small* **14**, 1703762 (2018).

30. Wang, Y. *et al.* Lead-free perovskite Cs2AgBiBr6@g-C3N4 Z-scheme system for improving CH4 production in photocatalytic CO2 reduction. *Appl. Catal. B Environ.* **282**, 119570 (2021).

31. Bibi, A. *et al.* Lead-free halide double perovskites: Toward stable and sustainable optoelectronic devices. *Materials Today* **49**, 123–144 (2021).

32. Creutz, S. E., Crites, E. N., De Siena, M. C. & Gamelin, D. R. Colloidal Nanocrystals of Lead-Free Double-Perovskite (Elpasolite) Semiconductors: Synthesis and Anion Exchange to Access New Materials. *Nano Lett.* **18**, 1118–1123 (2018).

33. Slavney, A. H., Hu, T., Lindenberg, A. M. & Karunadasa, H. I. A Bismuth-Halide Double Perovskite with Long Carrier Recombination Lifetime for Photovoltaic Applications. *J. Am. Chem. Soc.* **138**, 2138–2141 (2016).

34. Gao, W. *et al.* High-Quality Cs2AgBiBr6 Double Perovskite Film for Lead-Free Inverted Planar Heterojunction Solar Cells with 2.2 % Efficiency. *ChemPhysChem* **19**, 1696–1700 (2018).

35. Fan, P. *et al.* Single-source vapor-deposited Cs2AgBiBr6 thin films for lead-free perovskite solar cells. *Nanomaterials* **9**, (2019).

36. Liu, Z. *et al.* Synthesis of lead-free Cs2AgBix6 (X = Cl, Br, I) double perovskite nanoplatelets and their application in CO2 photocatalytic reduction. *Nano Lett.* **21**, 1620–1627 (2021).

37. Humayun, M., Wang, C. & Luo, W. Recent Progress in the Synthesis and Applications of Composite Photocatalysts: A Critical Review. *Small Methods* **6**, 2101395 (2022).

38. Xu, Y. F. *et al.* A CsPbBr3 Perovskite Quantum Dot/Graphene Oxide Composite for Photocatalytic CO2 Reduction. *J. Am. Chem. Soc.* **139**, 5660–5663 (2017).

39.   Kumar, S., Regue, M., Isaacs, M. A., Freeman, E. & Eslava, S. All-Inorganic CsPbBr3Nanocrystals: Gram-Scale Mechanochemical Synthesis and Selective Photocatalytic CO2Reduction to Methane. *ACS Appl. Energy Mater.* **3**, 4509–4522 (2020).

40.   Low, J., Yu, J., Jaroniec, M., Wageh, S. & Al-Ghamdi, A. A. Heterojunction Photocatalysts. *Advanced Materials* **29**, 1601694 (2017).

41.   Mishra, R. *et al.* A review on Z/S – scheme heterojunction for photocatalytic applications based on metal halide perovskite materials. *Applied Surface Science Advances* **9**, 100241 (2022).

42.   Bai, S., Jiang, J., Zhang, Q. & Xiong, Y. Steering charge kinetics in photocatalysis: Intersection of materials syntheses, characterization techniques and theoretical simulations. *Chem. Soc. Rev.* **44**, 2893–2939 (2015).

43.   Bard, A. J. Photoelectrochemistry and heterogeneous photo-catalysis at semiconductors. *J. Photochem.* **10**, 59–75 (1979).

44.   Yu, J., Wang, S., Low, J. & Xiao, W. Enhanced photocatalytic performance of direct Z-scheme g-C 3N4-TiO2 photocatalysts for the decomposition of formaldehyde in air. *Phys. Chem. Chem. Phys.* **15**, 16883–16890 (2013).

45.   Rowsell, J. L. C. & Yaghi, O. M. Strategies for hydrogen storage in metal-organic frameworks. *Angewandte Chemie - International Edition* **44**, 4670–4679 (2005).

46.   Millward, A. R. & Yaghi, O. M. Metal-organic frameworks with exceptionally high capacity for storage of carbon dioxide at room temperature. *J. Am. Chem. Soc.* **127**, 17998–17999 (2005).

47.   Yao, J. & Wang, H. Zeolitic imidazolate framework composite membranes and thin films: Synthesis and applications. *Chemical Society Reviews* **43**, 4470–4493 (2014).

48.   Lee, J. *et al.* Metal-organic framework materials as catalysts. *Chem. Soc. Rev.* **38**, 1450–1459 (2009).

49.   Dhakshinamoorthy, A., Alvaro, M. & Garcia, H. Commercial metal–organic frameworks as heterogeneous catalysts. *Chem. Commun.* **48**, 11275–11288 (2012).

50.   Qiu, J. *et al.* Modified metal-organic frameworks as photocatalysts. *Applied Catalysis B: Environmental* **231**, 317–342 (2018).

51.   Cavka, J. H. *et al.* A new zirconium inorganic building brick forming metal organic frameworks with exceptional stability. *J. Am. Chem. Soc.* **130**, 13850–13851 (2008).

52.   Lawrence, M. C., Schneider, C. & Katz, M. J. Determining the structural stability of UiO-67 with respect to time: a solid-state NMR investigation. *Chem. Commun.* **52**, 4971–4974 (2016).

53.   Øien-ØDegaard, S. *et al.* UiO-67-type Metal-Organic Frameworks with Enhanced Water Stability and Methane Adsorption Capacity. *Inorg. Chem.* **55**, 1986–1991 (2016).

54.   Lee, C. C., Chen, C. I., Liao, Y. Te, Wu, K. C. W. & Chueh, C. C. Enhancing Efficiency and Stability of Photovoltaic Cells by Using Perovskite/Zr-MOF Heterojunction Including Bilayer and Hybrid Structures. *Adv. Sci.* **6**, 1801715 (2019).

55.   Schaate, A. *et al.* Modulated synthesis of Zr-based metal-organic frameworks: From nano to single crystals. *Chem. - A Eur. J.* **17**, 6643–6651 (2011).

56.   Kaur, G. *et al.* Controlling the Synthesis of Metal-Organic Framework UiO-67 by Tuning Its Kinetic Driving Force. *Cryst. Growth Des.* **19**, 4246–4251 (2019).

57.   Gutov, O. V., Hevia, M. G., Escudero-Adán, E. C. & Shafir, A. Metal-Organic Framework (MOF) Defects under Control: Insights into the Missing Linker Sites and Their Implication in the Reactivity of Zirconium-Based

Frameworks. *Inorg. Chem.* **54**, 8396–8400 (2015).

58. Ragon, F. *et al.* In situ energy-dispersive x-ray diffraction for the synthesis optimization and scale-up of the porous zirconium terephthalate UiO-66. *Inorg. Chem.* **53**, 2491–2500 (2014).

59. Katz, M. J. *et al.* A facile synthesis of UiO-66, UiO-67 and their derivatives. *Chem. Commun.* **49**, 9449–9451 (2013).

60. Ali Raza, M., Li, F., Que, M., Zhu, L. & Chen, X. Photocatalytic reduction of CO 2 by halide perovskites: recent advances and future perspectives. **2**, 7187 (2021).

61. Bhosale, S. S. *et al.* Mechanism of Photocatalytic CO2 Reduction by Bismuth-Based Perovskite Nanocrystals at the Gas-Solid Interface. *J. Am. Chem. Soc.* **141**, 20434–20442 (2019).

62. Protesescu, L. *et al.* Nanocrystals of Cesium Lead Halide Perovskites (CsPbX3, X = Cl, Br, and I): Novel Optoelectronic Materials Showing Bright Emission with Wide Color Gamut. *Nano Lett.* **15**, 3692–3696 (2015).

63. Lu, C. *et al.* Cesium Oleate Precursor Preparation for Lead Halide Perovskite Nanocrystal Synthesis: The Influence of Excess Oleic Acid on Achieving Solubility, Conversion, and Reproducibility. *Chem. Mater.* **31**, 62–67 (2019).

64. Huang, Y., Tao, C. A., Chen, R., Sheng, L. & Wang, J. Comparison of fabrication methods of metal-organic framework optical thin films. *Nanomaterials* **8**, (2018).

65. Yang, Q. *et al.* High effective adsorption/removal of illegal food dyes from contaminated aqueous solution by Zr-MOFs (UiO-67). *Food Chem.* **254**, 241–248 (2018).

66. Yang, Q. *et al.* The simultaneous detection and removal of organophosphorus pesticides by a novel Zr-MOF based smart adsorbent. *J. Mater. Chem. A* **6**, 2184–2192 (2018).

67. Dong, X., Lin, Y., Ma, Y. & Zhao, L. Ce-doped UiO-67 nanocrystals with improved adsorption property for removal of organic dyes. *RSC Adv.* **9**, 27674–27683 (2019).

68. Pankajakshan, A., Sinha, M., Ojha, A. A. & Mandal, S. Water-Stable Nanoscale Zirconium-Based Metal-Organic Frameworks for the Effective Removal of Glyphosate from Aqueous Media. *ACS Omega* **3**, 7832–7839 (2018).

69. Firth, F. C. N. *et al.* Engineering new defective phases of UiO family metal-organic frameworks with water. *J. Mater. Chem. A* **7**, 7459–7469 (2019).

70. Huang, Y., Tao, C. A., Chen, R., Sheng, L. & Wang, J. Comparison of fabrication methods of metal-organic framework optical thin films. *Nanomaterials* **8**, (2018).

71. Thickett, D. & Pretzel, B. FTIR surface analysis for conservation. *Herit. Sci.* **8**, 1–10 (2020).

72. Ravi, V. K., Swarnkar, A., Chakraborty, R. & Nag, A. Excellent green but less impressive blue luminescence from CsPbBr3 perovskite nanocubes and nanoplatelets. *Nanotechnology* **27**, (2016).

73. Lin, Z. H. *et al.* Synthesis and model simulation of the hexagonal to circular transition of perovskite cesium lead halide nanosheets by rapidly changing the temperature. *RSC Adv.* **10**, 4211–4217 (2020).

74. Bekenstein, Y., Koscher, B. A., Eaton, S. W., Yang, P. & Alivisatos, A. P. Highly Luminescent Colloidal Nanoplates of Perovskite Cesium Lead Halide and Their Oriented Assemblies. *J. Am. Chem. Soc* **137**, 46 (2015).

75. Ding, L. *et al.* Assembling an Affinal 0D CsPbBr3/2D CsPb2Br5Architecture by Synchronously in Situ Growing CsPbBr3QDs and CsPb2Br5Nanosheets: Enhanced Activity and Reusability for Photocatalytic CO2Reduction.

ACS Appl. Mater. Interfaces **13**, 51161–51173 (2021).

76. Tang, X. *et al.* All-inorganic perovskite CsPb2Br5 microsheets for photodetector application. *Front. Phys.* **5**, 69 (2018).

77. Gao, G. *et al.* Novel inorganic perovskite quantum dots for photocatalysis. *Nanoscale* **9**, 12032–12038 (2017).

78. Jung, J. H., Kim, S. H., Park, Y., Lee, D. & Lee, J. S. Metal-Halide Perovskite Design for Next-Generation Memories: First-Principles Screening and Experimental Verification. *Adv. Sci.* **7**, (2020).

79. Zhou, L., Xu, Y. F., Chen, B. X., Kuang, D. Bin & Su, C. Y. Synthesis and Photocatalytic Application of Stable Lead-Free Cs2AgBiBr6 Perovskite Nanocrystals. *Small* **14**, 1703762 (2018).

80. Abiram, G. *et al.* Air processed Cs2AgBiBr6 lead-free double perovskite high-mobility thin-film field-effect transistors. *Sci. Rep.* **12**, 1–8 (2022).

81. Slavney, A. H., Hu, T., Lindenberg, A. M. & Karunadasa, H. I. A Bismuth-Halide Double Perovskite with Long Carrier Recombination Lifetime for Photovoltaic Applications. *J. Am. Chem. Soc.* **138**, 2138–2141 (2016).

82. Greul, E., Petrus, M. L., Binek, A., Docampo, P. & Bein, T. Highly stable, phase pure Cs2AgBiBr6 double perovskite thin films for optoelectronic applications. *J. Mater. Chem. A* **5**, 19972–19981 (2017).
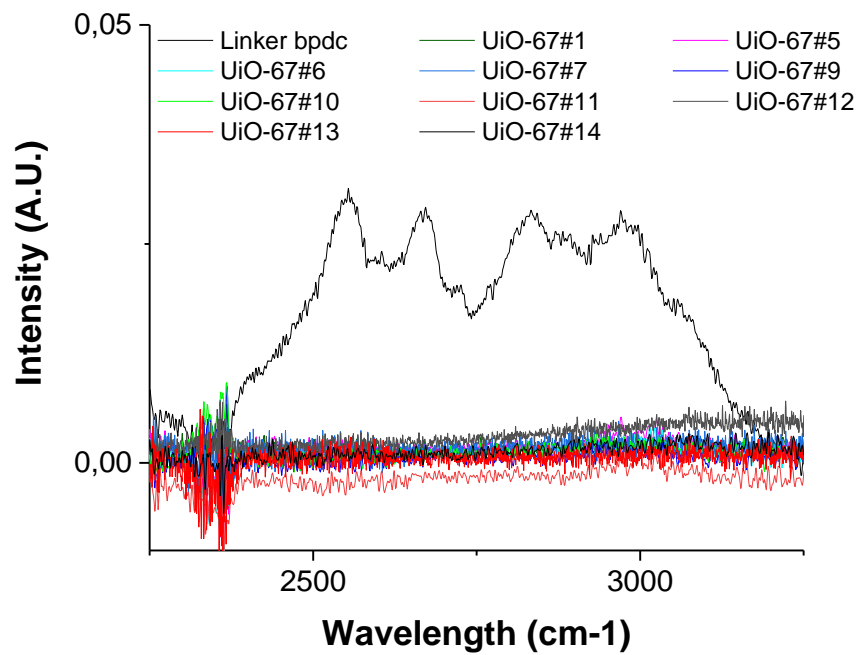
6- Appendix

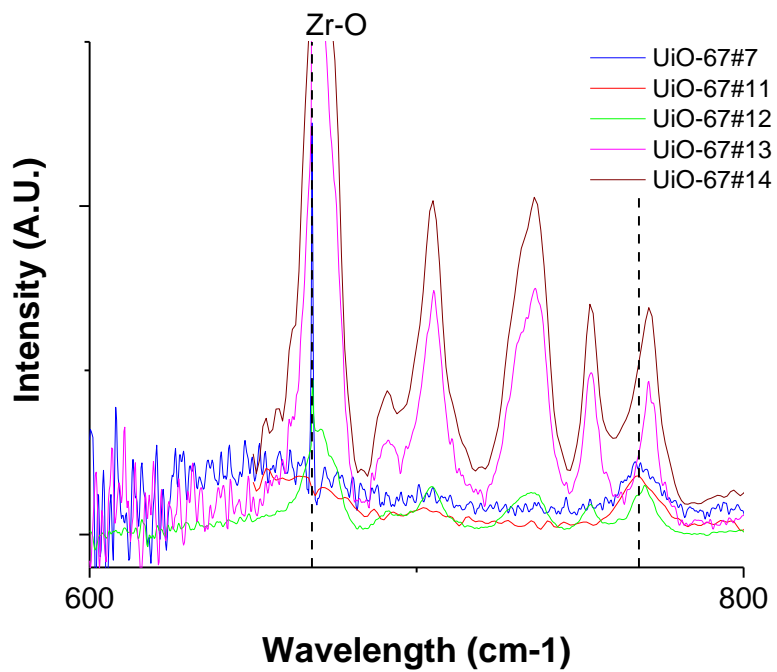*Figure A1: IR data of UiO-67 and the pure bpdc linker*
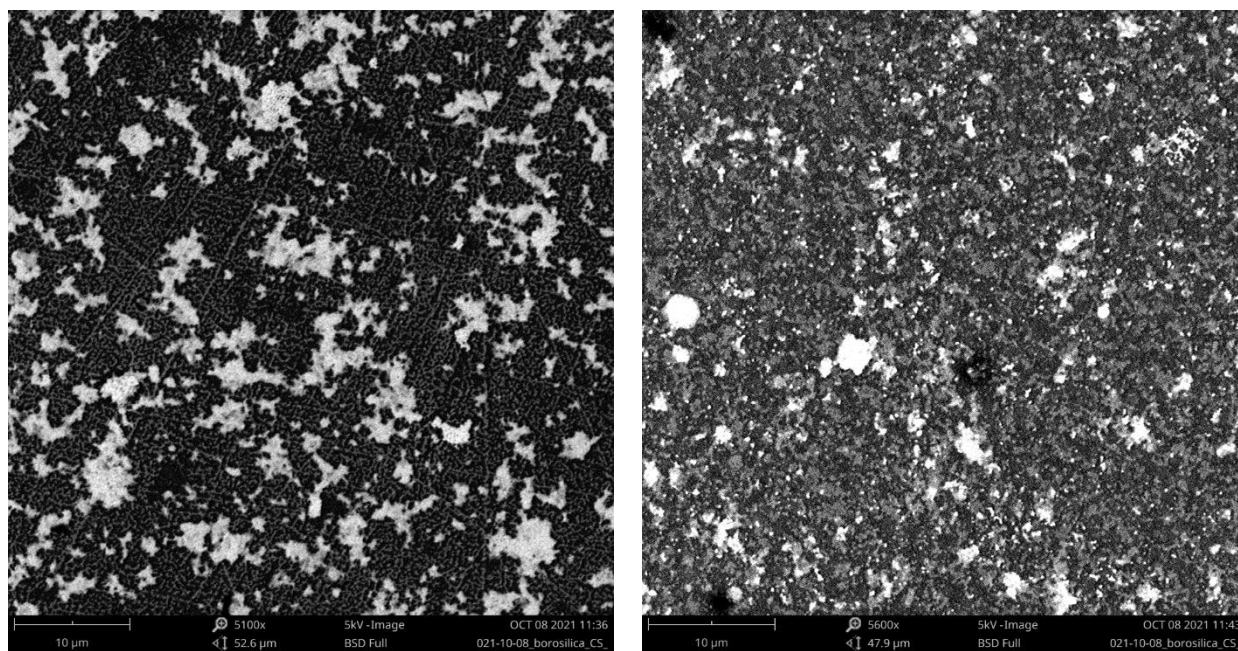
Figure A2: IR data of UiO-67 zoomed in

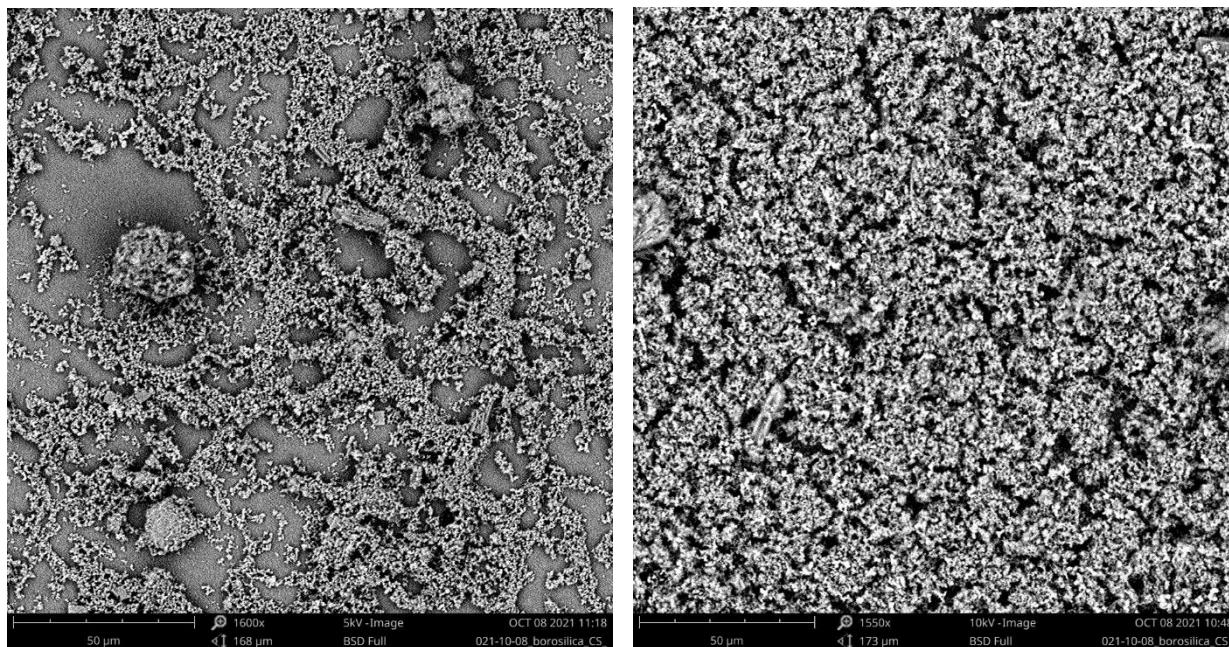*Figure A3: SEM images of spin coated CsPbBr₃ (left) and CABB (right) in toluene*

Figure A4: SEM images of UiO-67 spin coated in ethanol (left) and toluene (right)
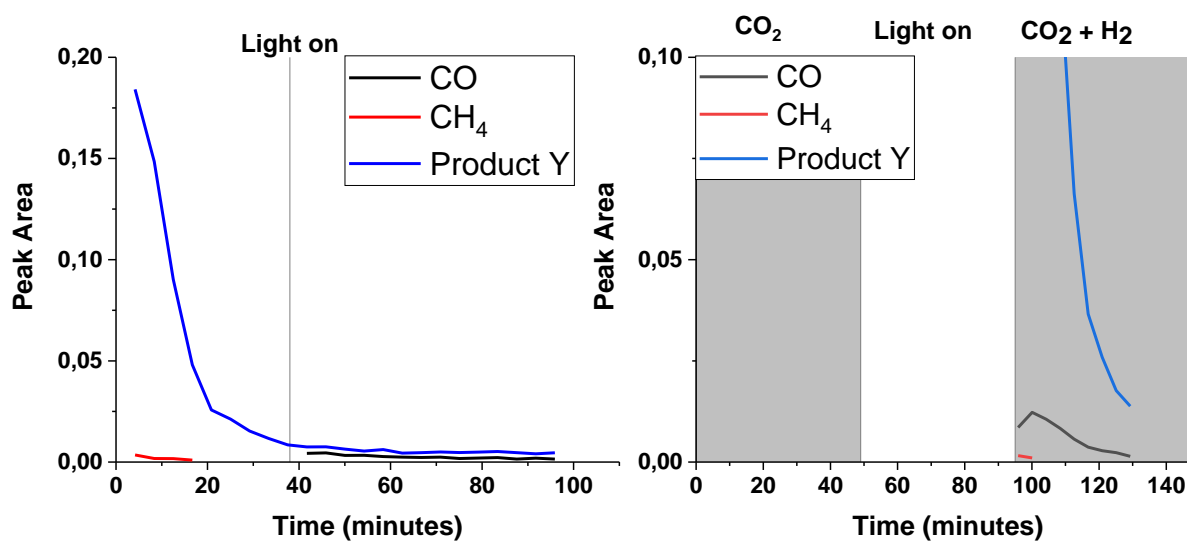

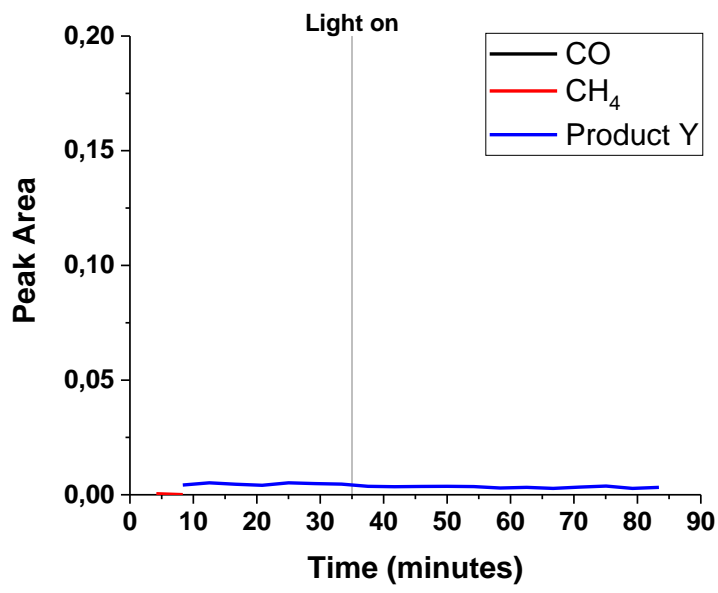*Figure A5: TiO$_2$ GC results (left) and the results with a H$_2$O bubbler (right)*

Figure A6: GC results of a clean wafer as a blanco experiment.